A&A 597, A130 (2017)
DOI: 10.1051/0004-6361/201629013

Astronomy & Astrophysics

The *Herschel* Virgo Cluster Survey

XX. Dust and gas in the foreground Galactic cirrus⋆,⋆⋆

S. Bianchi[1], C. Giovanardi[1], M. W. L. Smith[2], J. Fritz[3], J. I. Davies[2], M. P. Haynes[4], R. Giovanelli[4], M. Baes[5], M. Bocchio[6], S. Boissier[7], M. Boquien[8], A. Boselli[7], V. Casasola[1], C. J. R. Clark[2], I. De Looze[9], S. di Serego Alighieri[1], M. Grossi[10], A. P. Jones[6], T. M. Hughes[11], L. K. Hunt[1], S. Madden[12], L. Magrini[1], C. Pappalardo[13,14], N. Ysard[6], and S. Zibetti[1]

[1] INAF–Osservatorio Astrofisico di Arcetri, Largo E. Fermi, 5, 50125 Firenze, Italy
e-mail: sbianchi@arcetri.astro.it
[2] School of Physics and Astronomy, Cardiff University, Queens Building, The Parade, Cardiff, CF24 3AA, UK
[3] Instituto de Radioastronomía y Astrofísica, UNAM, Antigua Carretera a Pátzcuaro #8701, Morelia, Michoacán, Mexico
[4] Cornell Center for Astrophysics and Planetary Science, Space Sciences Bldg., Cornell University, Ithaca, NY 14853, USA
[5] Sterrenkundig Observatorium, Universiteit Gent, Krijgslaan 281-S9, 9000 Gent, Belgium
[6] Institut d'Astrophysique Spatiale (IAS), UMR 8617, CNRS/Université Paris-Sud, 91405 Orsay, France
[7] Aix Marseille Université, CNRS, LAM (Laboratoire d'Astrophysique de Marseille), UMR 7326, 13388 Marseille, France
[8] Unidad de Astronomia, Facultad de Ciencias Basicas, Universidad de Antofagasta, Avenida Angamos 601, 1270300 Antofagasta, Chile
[9] Dept. of Physics & Astronomy, University College London, Gower Street, London WC1E 6BT, UK
[10] Observatório do Valongo, Universidade Federal do Rio de Janeiro, Ladeira Pedro Antônio 43, Rio de Janeiro, Brazil
[11] Instituto de Física y Astronomía, Universidad de Valparaíso, Avda. Gran Bretaña 1111, Valparaíso, Chile
[12] Laboratoire AIM, CEA/DSM – CNRS – Université Paris Diderot, IRFU/Service d'Astrophysique, CEA Saclay, 91191 Gif-sur-Yvette, France
[13] Instituto de Astrofísica e Ciências do Espaço, Universidade de Lisboa, Tapada da Ajuda, 1349-018 Lisboa, Portugal
[14] Observatório Astronómico de Lisboa, Tapada da Ajuda, 1349-018 Lisboa, Portugal

Received 27 May 2016 / Accepted 19 September 2016

ABSTRACT

We study the correlation between far-infrared/submm dust emission and atomic gas column density in order to derive the properties of the high Galactic latitude, low density, Milky Way cirrus in the foreground of the Virgo cluster of galaxies. Dust emission maps from 60 to 850 μm are obtained from observations with the Spectral and Photometric Imaging Receiver (SPIRE) and carried out within the *Herschel* Virgo Cluster Survey (HeViCS); these are complemented by IRAS and *Planck* maps. Data from the Arecibo legacy Fast ALFA Survey is used to derive atomic gas column densities for two broad velocity components: low and intermediate velocity clouds. Dust emissivities are derived for each gas component and each far-infrared/submm band. For the low velocity clouds, we measure an average emissivity $\epsilon_\nu^{\rm LVC} = (0.79 \pm 0.08) \times 10^{-20}$ MJy sr^{-1} cm^2 at 250 μm. After fitting a modified blackbody to the available bands, we estimated a dust absorption cross section of $\tau_\nu^{\rm LVC}/N_{\rm H\,I} = (0.49 \pm 0.13) \times 10^{-25}$ cm^2 H^{-1} at 250 μm (with dust temperature $T = 20.4 \pm 1.5$ K and spectral index $\beta = 1.53 \pm 0.17$). The results are in excellent agreement with those obtained by *Planck* over a much larger coverage of the high Galactic latitude cirrus (50% of the sky versus 0.2% in our work). For dust associated with intermediate velocity gas, we confirm earlier *Planck* results and find a higher temperature and lower emissivity and cross section. After subtracting the modeled components, we find regions at scales smaller than 20′ in which the residuals deviate significantly from the average scatter, which is dominated by cosmic infrared background. These large residuals are most likely due to local variations in the cirrus dust properties or to high-latitude molecular clouds with average $N_{\rm H_2} \lesssim 10^{20}$ cm^{-2}. We find no conclusive evidence for intracluster dust emission in Virgo.

Key words. dust, extinction – radiation mechanisms: thermal – infrared: ISM – submillimeter: ISM – radio lines: ISM – local insterstellar matter

1. Introduction

Diffuse far-infrared (FIR) emission from high-Galactic latitude dust (the Milky Way cirrus) is an important test bed for models of interstellar grains. The thinness of the Galactic disk, our peripheric position in this disk, and a viewing direction away from the Galactic plane offer clear advantages to modeling. The main source of dust heating is provided by the ambient radiation, i.e., the local interstellar radiation field (LISRF; Mathis et al. 1983) because the diffuse radiation gradients perpendicular to the disk are small, as shown by radiative transfer models of Galactic disks (Bianchi et al. 2000; Bocchio et al. 2013; Popescu & Tuffs 2013). Thus the mixing of dust at different temperatures, or with different properties, along a single line of sight is limited.

⋆ *Herschel* is an ESA space observatory with science instruments provided by European-led Principal Investigator consortia and with important participation from NASA.
⋆⋆ Final reduced data (FITS) are only available at the CDS via anonymous ftp to cdsarc.u-strasbg.fr (130.79.128.5) or via http://cdsarc.u-strasbg.fr/viz-bin/qcat?J/A+A/597/A130

Starting from the first detection of the cirrus emission by the IRAS satellite (Low et al. 1984), a tight correlation of the FIR surface brightness with the atomic gas column density was observed (Boulanger & Perault 1988). The cirrus surface brightness per H I column density (a quantity known as emissivity) measured in the 60 and 100 μm IRAS bands was then used to verify the predictions or constrain the properties of early interstellar grain models (Draine & Lee 1984; Désert et al. 1990).

With the advent of the instruments aboard the COBE satellite, and in particular the Far Infrared Absolute Spectrophotometer (FIRAS), it was possible to study the spectral energy distribution (SED) of the cirrus up to the peak of thermal emission and beyond. Boulanger et al. (1996) found a tight correlation with H I column density and measured the emissivity up to 1 mm. After fitting a modified blackbody (MBB) to the data, the dust absorption cross section per unit H I column density was retrieved, which was found to be in agreement with the available dust models. Since then, the FIRAS emissivity has been one of the major constraints to dust models, which were formulated to reproduce its SED levels and shape, resulting in an average dust cross section, $\propto \nu^{\beta}$, with $\beta \approx 1.8{-}2$ (see, e.g., Draine 2003; Zubko et al. 2004; Compiègne et al. 2011; Jones et al. 2013).

The recent analysis of data from the *Planck* satellite, however, revealed an inconsistency between *Planck* and FIRAS, which prompted a recalibration on planet fluxes of the 350 and 550 μm data from the High Frequency Instrument (HFI; Planck Collaboration VIII 2014). As a result, the newly determined emissivities have been found to be lower than the FIRAS values, and with a reduced dust cross-section spectral index ($\beta \approx 1.6$; Planck Collaboration XI 2014; Planck Collaboration Int. XVII 2014). These results suggest that a re-evaluation of the dust model parameters may be required, in particular, of the grain size distributions and relative contribution of grains of different chemical composition to the SED at 100 μm $\lesssim \lambda \lesssim$ 1 mm. Furthermore, the higher resolution of *Planck* data with respect to FIRAS highlighted local dust emissivity variations with the environment (Planck Collaboration XI 2014; Planck Collaboration Int. XVII 2014).

A tenuous cirrus is seen in the foreground of the Virgo cluster of galaxies ($l = 283.8°, b = 74.4°$) through scattered starlight in deep optical (Rudick et al. 2010; Mihos 2015) and UV images (Cortese et al. 2010; Boissier et al. 2015); it corresponds to low extinction with $0.02 < E(B-V) < 0.1$ (Boissier et al. 2015). Its emission is clearly detected at 250, 350, and 500 μm in images obtained by the Spectral and Photometric Imaging Receiver (SPIRE; Griffin et al. 2010) aboard the *Herschel* Space Observatory (Pilbratt et al. 2010), as part of the *Herschel* Virgo Cluster Survey (HeViCS; Davies et al. 2010a, 2012; Auld et al. 2013). In this work, we derive the dust emissivity of the HeViCS cirrus in the SPIRE bands. This allows us to verify the latest *Planck* results, since the SPIRE calibration also is based on planet models. Besides, the 250 μm band fills the gap between the IRAS and *Planck* data, and complements the lower sensitivity and resolution COBE-DIRBE emissivity at 240 μm (Planck Collaboration Int. XVII 2014). When compared to the *Planck* large area estimates, the relatively small sky coverage of the HeViCS field also highlights local emissivity variations.

The emissivities are derived using H I observations from the Arecibo Legacy Fast ALFA survey (ALFALFA), exploiting ALFA, the Arecibo *L*-band Feed Array (Giovanelli et al. 2005). The high resolution of the ALFALFA data (*FWHM* = 3.′5) is comparable to that of the longest wavelength data dominated by dust thermal emission (the 850 μm *Planck*-HFI band, with 4.′8); it is also a factor two better than other H I data used to derive dust emissivities: previous large-area studies (Boulanger et al. 1996; Planck Collaboration XI 2014) used observations at *FWHM* = 0.6° from the Leiden/Argentine/Bonn (LAB) Survey of Galactic H I (Kalberla et al. 2005). The *FWHM* = 14.′5 Galactic All Sky Survey of the southern hemisphere has been used in Planck Collaboration Int. XVII (2014), while Planck Collaboration XXIV (2011) exploited Green Bank Telescope maps at *FWHM* = 9.′1. Only in the recent work of Reach et al. (2015) Arecibo telescope data from the Galactic ALFA (GALFA; Peek et al. 2011) survey have been used to study the correlation between H I column density of isolated high-latitude clouds and *Planck*-based dust column densities.

The resolution of the ALFALFA survey thus allows a characterization of the residuals to the dust-H I correlation at smaller scales. In fact, one of the aims of HeViCS is the detection of dust emission from the intracluster medium (ICM), once the structure of the foreground cirrus is subtracted using Galactic H I as a template. The presence of the cirrus is indeed the limiting factor in these studies. So far the only claim of the detection of FIR emission from the ICM is that on the Coma cluster by Stickel et al. (1998), using data from the ISO satellite. However, the analysis of five other clusters with analogous data and techniques yielded no detection (Stickel et al. 2002); a following analysis of Coma using data from the *Spitzer* satellite dismissed the putative emission as cirrus contamination (Kitayama et al. 2009).

This paper is organized as follows: in Sect. 2 we present the ALFALFA and HeViCS data, together with other ancillary maps used in this work. In Sect. 3 we describe the method used to derive the correlation between dust and H I. The fitted emissivities are presented in Sect. 4, while Sect. 5 is dedicated to the derivation of the mean opacity cross section from the emissivity SEDs. The possible Galactic origin of the largest residuals is discussed in Sect. 6, while in Sect. 7 we put constrains on the dust emission from the Virgo ICM. The work is summarized in Sect. 8.

2. Data sets

The HeViCS project obtained FIR/submm images of about 84 deg^2 over the Virgo cluster, using the photometers aboard *Herschel*. The survey area was covered with four overlapping fields. The survey strategy and observations are described in detail in several previous publication of the HeViCS series (e.g., Davies et al. 2010a, 2012; Auld et al. 2013).

In this section we describe the H I and FIR/submm data sets we used to derive the emissivity of MW dust in the HeViCS footprint.

2.1. H I *ALFALFA data*

The ALFALFA (Giovanelli et al. 2005) is a spectrophotometric, wide-field survey at the Arecibo radio telescope aimed to deliver the properties of galaxies in the local Universe, as revealed by the 21 cm line of interstellar atomic hydrogen. This survey covers a spectral range of 100 MHz with a resolution of 25 kHz (~5.1 km s), including the spectral domain of interstellar and perigalactic emission. It uniformly covers the sky footprint of the HeViCS survey, with an angular resolution of 3.5′ *FWHM*. We took the data in drift mode, i.e., with the telescope scanning tracks of constant declination at the sidereal rate. Two independent polarization components of the data are recorded. Basic data units are 3D. Each data cube is complemented by a 2D map of the continuum background and a 3D array carrying the data quality of each pixel.

The use of the ALFALFA data for this work requires two important differences in the generation of the data cubes with respect to the pipeline processing adopted for extragalactic applications: first, the spectral stretch of the data cubes is restricted to the range between −1000 and +1050 km s, which includes 400 spectral channels spaced by 25 kHz (5.1 km s); and, second, the flux scale is calibrated in Kelvin degrees of antenna temperature T_A. The sky footprint of each cube retains the same size as the standard ALFALFA data cubes, i.e., 2.4° × 2.4°, sampled at 1′ pixel separation. The array dimensions of each data cube are then 400 × 2 × 144 × 144, where the "2" refers to the two polarization channels. Each of the four HeViCS fields is fully covered by ten ALFALFA data cubes with significant coverage overlap; each point in the HeViCS sky footprint is contained in at least two different ALFALFA data cubes.

We then proceeded to the baselining. For each grid and for each polarization, we assembled all the spectra at a given declination in an image, thus obtaining the equivalent of a longslit image. Upon inspection of the central 1000 km s^{-1}, and excluding the range occupied by the Galactic line at levels over the noise, we fitted to each spectrum and then removed a polynomial baseline of order up to 6. During this phase we also removed from the "longslit" images any striping due to residual RFI or autocorrelator faults. The processing pipeline was satisfactory overall, except for lines of sight within 15′ of the center of galaxy M 87, where the strong continuum emission of Virgo A drastically increases noise and associated standing waves makes spectral baselining impossible.

The next phase was the flatfielding of the channel maps. We assembled the grid data for each velocity channel into a different map separately for the two polarizations again. These maps were singly inspected and, if required, corrected for residual striping or stepping at the junction between different drifts. The flatfielding procedure was repeated twice: first to eliminate the most obvious defects, and then again for refinement and a double check of the results.

Finally we used an IDL procedure to produce, for each grid, FITS 2D images of the single fully reduced channel maps, or of a velocity range of choice; such a procedure also averages the two polarizations. The `swarp` software (Bertin et al. 2002) was used to mosaic the FITS output for the grids into maps covering each single HeViCS field and the whole HeViCS footprint. The final maps were converted into units of main beam temperature.

In order to check the H I 21 cm line optical depths in the area, we selected from the NVSS catalog (Condon et al. 1998) all 1400 MHz radio sources with a flux density in excess of 500 mJy located within the HeViCS footprint. This flux limit was computed, given the noise figures of the ALFALFA spectra, to ensure a clear detection ($S/N > 5$) of absorption features from column densities $N_{HI} > 5 \times 10^{18}$ cm^{-2} with average conditions for spin temperature (100 K) and velocity dispersion (5 km s^{-1}). We rejected those sources located within 20′ of M 87, and those not isolated enough or extended, ending up with a list of 22 objects. For each source, the central spectrum was obtained by summing the spectra within a radius of 3′. The emission spectrum was estimated as the median of six similar apertures surrounding the central source at distance of 10′ in a hexagonal pattern. The absorption spectrum was derived by subtracting the emission spectrum from the central spectrum, and was analyzed using standard techniques (see, e.g., Spitzer 1978). Absorption was detected in all 22 spectra, sometimes with multiple features. The optical depths, which we derive with uncertainty of ∼0.003, span from 0.01 to 0.4 but with an average of only 0.058 ± 0.058; their distribution is illustrated in Fig. 1. The spin temperatures,

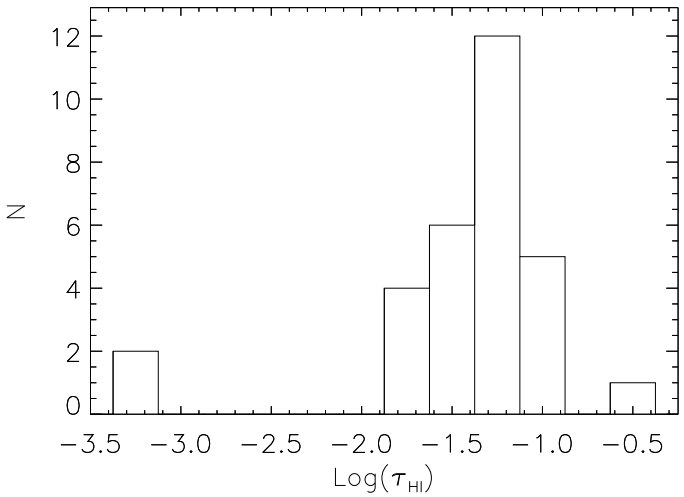

Fig. 1. Distribution histogram of the 21 cm line opacity computed for the 30 absorption features detected on the line of sight to NVSS continuum radio sources.

measured with uncertainty of ∼10 K, are low, between 50 and 100 K, with only one case exceeding 150 K; their mean value is 55 ± 28 K. The H I column densities range between 2×10^{18} and 2×10^{20} cm^{-2}, with a log mean of 19.60 ± 0.54. Given that the peak brightness temperature of the line is around 3 K and the noise in the spectra is 0.003 K, even taking into account the error in the optical depth corrections, the uncertainty in the total column density is always better than 4%. The average correction factor for optical thickness is 1.021 ± 0.029; consequently, throughout the paper, we derived the H I column densities at the optically thin limit.

Planck Collaboration XXIV (2011) has shown that the H I emission can be decomposed into various velocity components by inspecting the channel-to-channel variations of the median and of the standard deviation; the second in particular is more sensitive to structure variation across the field. In Fig. 2 we plot these median and standard deviation spectra for the full HeViCS field. The standard deviation spectrum shows that there are two components, partially overlapping in velocity at $v_{LSR} \approx -20$ km s^{-1}. Following the approach of Planck Collaboration XXIV (2011), we thus produced two separate maps of column density using

$$N_{HI} = 1.823 \times 10^{18} \sum T_b(v)\Delta v \text{ cm}^{-2},$$

with T_b the main beam temperature spectrum for each pixel. The summation was extended over the velocity range $-20 \lesssim v_{LSR}$ (km s^{-1}) $\lesssim 100$ for low velocity clouds (LVC); over $-100 \lesssim v_{LSR}$ (km s^{-1}) $\lesssim -20$, for intermediate velocity clouds (IVC). No other significant velocity components are found in the HeViCS field: in particular, there are no conspicuous high velocity clouds at the Galactic latitude of Virgo (see, e.g., Fig. 1 in Wakker & van Woerden 1997) and indeed the velocity channels in the range $-200 \lesssim v_{LSR}$ (km s^{-1}) $\lesssim -100$ are devoid of large-scale emission features.

We verified the consistency of the column density values measured on our ALFALFA map with those from the LAB survey (Kalberla et al. 2005). In particular, the Arecibo telescope is known to have significant stray-radiation contamination, which can affect the precise determination of the total column densities of large-scale features (see, e.g., Peek et al. 2011). Instead, the LAB data is corrected for stray radiation. We checked the contamination of the ALFALFA map by smoothing it to the

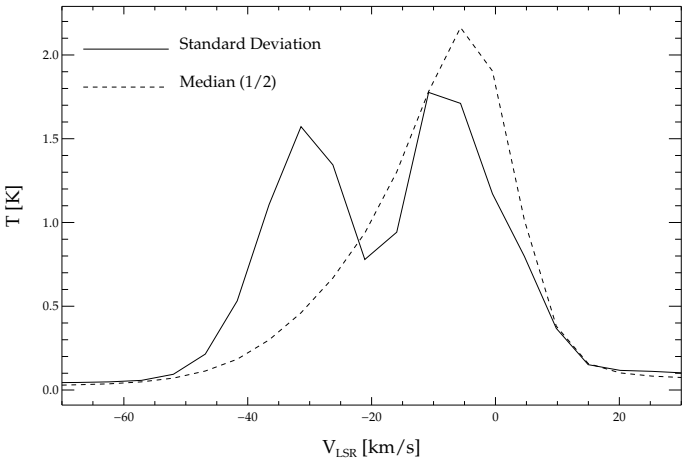

Fig. 2. Standard deviation (solid line) and median (dashed line) ALFALFA spectra for the HeViCS field. The median spectrum was divided by two for ease of presentation.

LAB resolution and performing a linear correlation between the column densities of the two data sets, for both the LVC and IVC channels. We found that the ALFALFA map of the LVC channel has a positive offset of 3.4×10^{19} cm^{-2} with respect to LAB, and a gain of close to unity, 1.06. For the IVC channel, the gain is higher (1.16) and the offset is smaller (1.3×10^{19} cm^{-2}). Since in this work we compared our determination of dust emissivities with those obtained using the LAB (Planck Collaboration VIII 2014; Planck Collaboration XI 2014), we corrected our maps for those offsets and gains. We comment on these corrections in Sect. 4.

2.2. HeViCS SPIRE images

Images at 250, 350, and 500 μm were obtained using the SPIRE instrument (Griffin et al. 2010) aboard *Herschel*. The SPIRE data were reduced using the dedicated software HIPE, version 11 (Ott 2010) and following the recommended procedures for maps of extended emission[1]. In previous HeViCS papers we used a custom method for the temperature drift correction and residual baseline subtraction (Bright Galaxy Adaptive Element – BriGAdE; Smith 2012), which is optimized for galaxies. For the larger scale of the cirrus emission, however, BriGAdE tends to flatten the surface brightness gradients. Thus, for the work of this paper we preferred to use the standard *destriper* available within HIPE, adopting a constant offset for each bolometer.

Because of memory limitations and of the relatively small overlap of the four tiles of which the survey is composed, it was not possible to run the *destriper* on the full HeViCS area. In any case, we have preferred to conduct our analysis on the individual fields, to study possible variations of the dust properties across the survey area. This also minimizes the impact of larger scale gradients resulting from diffuse Galactic emission and zodiacal light, which are poorly sampled by our limited-sized tiles. As SPIRE is only sensitive to relative field variations, each field is offset from the others because of their different median surface brightness levels. While it is possible to set an absolute flux offset by correlating *Herschel* and *Planck* observations within HIPE, we retained the original levels and relied on our own determination of the zero levels with respect to H I column density (see Sect. 3).

Images were created in Jy/beam with pixel sizes of 6, 8, and 12″ at 250, 350, and 500 μm. These values are about 1/3 of the main beam FWHM, which, for the adopted pixel sizes, is about 18, 24.5, and 36″. Units were finally converted to MJy sr^{-1}. The calibration uncertainty is 7% at all SPIRE wavelengths, including uncertainties in the model, measurements of the calibrator flux, and estimate of the beam areas.

We did not use the Photoconductor Array Camera and Spectrometer (PACS; Poglitsch et al. 2010) data taken in parallel with SPIRE. The cirrus is indeed detected at very faint levels at 160 μm, but the images contain large-scale artifacts of the data reduction process that prevented their usage.

2.3. IRAS and Planck

We used 60 and 100 μm maps from the IRAS satellite (Neugebauer et al. 1984). Images in MJy sr^{-1} with pixels size 1.′5 were obtained using the data set and procedures from the *Improved Reprocessing of the IRAS Survey* (IRIS; Miville-Deschênes & Lagache 2005). The PSF of the IRIS maps is estimated to be Gaussian, where FWHM is 4.′0 and 4.′3 at 60 and 100 μm, respectively. At both wavelengths, calibration uncertainties amount to about 15% and results from the uncertainties in the gain and color correction with respect to data from the poorer resolution, better photometric accuracy DIRBE instrument on the COBE satellite, which was used to recalibrate the IRAS data.

Maps at 350, 550, and 850 μm (857, 545, and 353 GHz, respectively) produced by the High Frequency Instrument (HFI) aboard the *Planck* satellite were taken from the 2013 data release (Planck Collaboration I 2014). These channels are dominated by foreground dust emission; the 850 μm map allows us to extend the analysis to longer wavelengths than those covered by SPIRE, while the maps at 350 and 550 μm provide a consistency check between SPIRE and HFI (and in general, a sanity check with the analysis in Planck Collaboration XXIV 2011; and Planck Collaboration XI 2014). We used the data corrected for Zodiacal emission, and regridded these data from the original HEALpix format to a RA/Dec frame centered on the HeViCS field.

While maps at 350 and 550 μm are already provided in MJy sr^{-1}, the map at 850 μm was converted into those units by multiplying the data by the band-average unit conversion coefficient as described in Planck Collaboration IX (2014). The map at 850 μm was found to be significantly contaminated by the cosmic microwave background (CMB). A few *Planck*-based models of the CMB are available, obtained with different methods (Planck Collaboration XII 2014). We first used the CMB model produced with the leading method, SMICA, which was found successful in subtracting the CMB contamination from maps of M 31 (Planck Collaboration Int. XXV 2015). However, in the SMICA map the CMB fluctuations are not defined in an aperture of 1° around M 87; large residuals are left in the area after the subtraction, which affect the derivation of the 850 μm emissivity in field V2. Thus, we preferred the NILC model, which shows CMB features also close to M 87. For the CMB subtraction (and emissivity analysis) in the other HeViCS fields, the use of the NILC map produces equivalent results to SMICA.

The PSF of *Planck* images can be described by Gaussians with FWHM very similar to those of IRAS at 4.′3, 4.′7 and 4.′8 at 350, 550, and 850 μm, respectively (Planck Collaboration I 2014). Calibration uncertainties are

[1] For information on the adopted calibration, beam sizes, and color corrections, see the SPIRE Handbook v.2.5 (2014), available at the *Herschel* Astronomers' website.

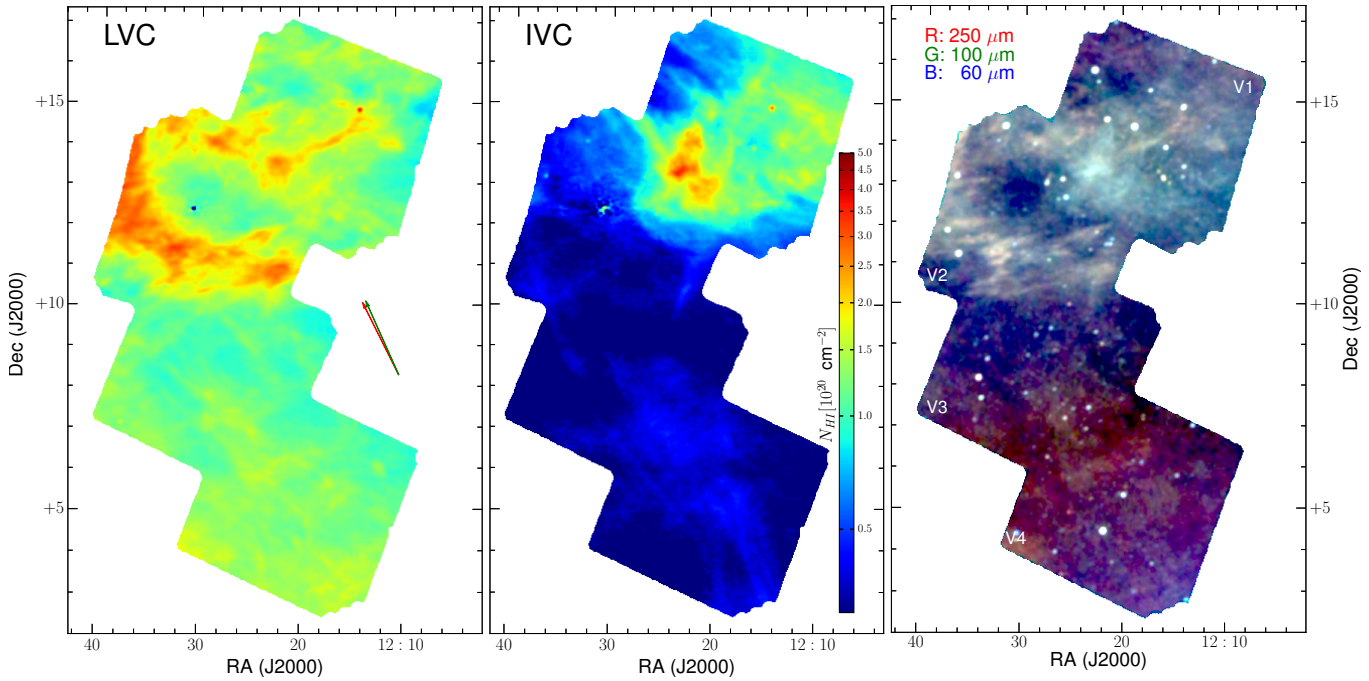

Fig. 3. HeViCS field: ALFALFA H I column density of the LVC component with $-20 < v_{LSR}/\mathrm{km\,s^{-1}} < 100$ (*left panel*), and of the IVC component with $-100 < v_{LSR}/\mathrm{km\,s^{-1}} < -20$ (*central panel*). Both components are shown with the same color scale. The RGB composite in the *right panel* shows dust emission at 60 μm (blue), 100 μm (green), and 250 μm (red). All images are convolved to a resolution of FWHM 4.′8. For this figure, the full 250 μm map was obtained by removing the mutual offsets between the HeViCS fields; the quantitative analysis is instead performed separately on each of the four fields, as motivated in Sect. 2.2. In the *left panel*, the red and green arrows indicate the direction of the Galactic and ecliptic north, respectively.

of 1% for the CMB calibrated 850 μm maps, and 10% for the two shorter wavelengths maps, whose calibration is based on planets: in the latter case the calibration uncertainty is not completely uncorrelated to that of SPIRE, both sharing a 5% uncertainty in the model flux of one of the HFI calibrators, the planet Neptune (Planck Collaboration VIII 2014).

2.4. Convolved and regridded maps

For each of the HeViCS fields (named V1, V2, V3 and V4 from north to south) we regridded all data sets to a common J2000 RA and Dec frame in gnomonic projection, with pixels size 1.′5. All maps were convolved to the poorer resolution of *Planck* 850 μm (4.′8) using simple Gaussian kernels. Excluding border regions with incomplete PSF sampling, the total area analyzed amounts to 76 deg^2 (64 deg^2 when excluding the masked sources). In Fig. 3 we show the gas column density of the LVC component (left panel), the IVC component (central panel), and an RGB representation of dust emission (right panel) of the full HeViCS area.

The left panel of Fig. 3 shows that LVC gas is present in all the HeViCS tiles. It is more diffuse in the southernmost fields V3 and V4 with an average column density $N_{\mathrm{H\,I}} = 1.2 \times 10^{20}$ cm^{-2}. Most of the gas is in the ring-like structure of field V2, coincidentally centered on the center of the Virgo cluster, where the peak column density is 3.3×10^{20} cm^{-2}. A long filament is the main structure in the center of field V1. The artifacts from M 87 (see Sect. 2.1) are visible as a lower than average column density feature in field V2, while the bright point source present in field V1 is the Virgo spiral NGC 4192 (M98) with Heliocentric radial velocity -139 km s^{-1} and velocity width $W_{50} = 461$ km s^{-1} (Giovanelli et al. 2007). Both NGG4192 and the artifacts from M 87 can be seen also in IVC maps.

Most of the IVC component (central panel) is instead concentrated in field V1 and V2 with a peak column density $N_{\mathrm{H\,I}} = 3.5 \times 10^{20}$ cm^{-2} in the overlap of the two tiles. This region corresponds to a column density enhancement at the border of a loose cloud known as *clump S1*, which is part of a larger Galactic structure named *Intermediate-Velocity (IV) Spur* (Kuntz & Danly 1996). The analysis of interstellar absorption lines toward the direction of the IV Spur has shown that this gas resides at a large distance from the Galactic plane with a distance bracket between 0.3 and 2.1 kpc (Kuntz & Danly 1996; Wakker 2001). Because of this structure, the average column density of the IVC component in field V1 is comparable to that of LVC ($N_{\mathrm{H\,I}} = 1.1 \times 10^{20}$ vs. 1.4×10^{20} cm^{-2}, respectively). Fields V3 and V4 instead have a tenuous IVC component with an average column density $N_{\mathrm{H\,I}} = 3.2 \times 10^{19}$ cm^{-2}. Also, in these fields IVC and LVC show a larger overlap in velocity space, and our simple v_{LSR} cut cannot provide a clear separation of the two components.

The RGB map in the right panel of Fig. 3 shows the overall correlation between dust and atomic gas: in particular, the ring-like feature of field V2 is also visible in dust emission (as it is in UV scattered light; Boissier et al. 2015). Also, dust emission associated with IVC gas appears to be bluer than that coming from LVC gas. The correlation is also evident in fields V3 and V4, where dust emission is tenuous.

3. Analysis

Our analysis follows the approach of the Planck Collaboration XXIV (2011). The surface brightness map of dust emission at frequency ν, I_ν, can be written as

$$I_\nu = \epsilon_\nu^{\mathrm{LVC}} \times N_{\mathrm{H\,I}}^{\mathrm{LVC}} + \epsilon_\nu^{\mathrm{IVC}} \times N_{\mathrm{H\,I}}^{\mathrm{IVC}} + O_\nu + E_\nu \times (b - b_0) + R_\nu, \quad (1)$$

where $N_{\rm H\,I}^{\rm LVC}$ and $N_{\rm H\,I}^{\rm IVC}$ are the H I column density maps for the low and intermediate velocity cloud components, respectively, and $\epsilon_\nu^{\rm LVC}$ and $\epsilon_\nu^{\rm IVC}$ are the emissivities of dust associated to these components. As (most of) the dust emission maps have a relative calibration, the absolute surface brightness levels are unknown; thus, the term O_ν is used to describe an offset (or *zero-level*), which also includes any large-scale contribution that is not directly correlated to the atomic gas. Since SPIRE images are not corrected for zodiacal light, and other data might have residual contributions from this foreground, we also included a term E_ν to describe a gradient in ecliptic latitude b, where b_0 is the central latitude in each map. The analysis consists in fitting the first four terms in right-hand side of Eq. (1) to the observed surface brightness I_ν. The last term in Eq. (1), R_ν, is the map of the residuals, i.e., the difference between the observed and modeled surface brightness.

In Eq. (1) we neglected the contribution of ionized gas, for which there is no available data at a comparable angular scale. Available, larger scale, Hα surveys (Haffner et al. 2003; Finkbeiner 2003) only show diffuse low-level features in the HeViCS footprint, which are barely correlated to our H I and dust emission maps. Converting the Hα intensities to ionized gas column densities (as in Lagache et al. 2000), we estimated that, within each field, the local column density can differ from the field average by up to $N_{\rm H\,II} \approx 3\times10^{19}$ cm^{-2}. While the dust emission associated with the average values would be hidden in O_ν, we predicted localized emission to be on the order of the standard deviation of the residuals to our fit, assuming similar dust properties in the neutral and ionized gas (Lagache et al. 1999, 2000). The contribution is probably smaller, since a significant portion of high-latitude Hα emission could be due to scattered light rather than to ionized gas (Witt et al. 2010). Thus, dust associated with ionized gas could contribute to the scatter in the $I_\nu/N_{\rm H}$ correlation, but it is not likely to produce any large deviation from the assumed model.

The model parameters were estimated using the IDL function `regress`, which performs a multiple linear regression fit. Fits were carried out separately for each of the HeViCS fields. We thus obtain, for each band, four values for each of the parameters, $\epsilon^{\rm LVC}$, $\epsilon^{\rm IVC}$, O_ν, E_ν. We excluded the regions with significant FIR emission from extragalactic sources from the fits, by masking circular apertures of diameter $4 \times FWHM$ around the brightest ($F > 1.1$ Jy) IRAS point sources (Helou & Walker 1988). The flux limit was selected to keep the masked areas to a reasonable size; later in Sect. 6 we discuss the effect of other unmasked sources on the residuals. Another mask was devised to exclude large deviations from the assumed model; after a first fit was performed to the high signal-to-noise 250 μm data, we inspected the probability distribution function (PDF) of R_ν and, by fitting a Gaussian to it, estimated the standard deviation of the residuals $\sigma_{\rm R}$. This second mask thus excludes all pixels in which residuals at 250 μm are $>3\sigma_{\rm R}$.

Since the fluctuations in residual maps do not behave as white noise, mainly because of the contribution of the cosmic infrared background (CIB), the parameter uncertainties derived from the fit are underestimated (see Planck Collaboration XXIV 2011, for a discussion). Thus, we estimated the uncertainties using a Monte Carlo technique. Simulated images were created starting from mock maps of the residuals with the same power spectra of R_ν, but with random phases, to which the other terms in Eq. (1) were added, using the observed hydrogen column density maps and the parameters estimated by the fit. The linear regression was repeated on the simulated images, after adding random representations of the instrumental noise to I_ν and the two column density maps. The procedure was repeated a thousand times, and a standard deviation was retrieved from the resulting PDFs of each of the four parameters. The instrumental noise used in this process was estimated on the convolved and regridded FIR/submm images by measuring the standard deviation of difference maps: for IRAS, we used the difference between observations of the first and second surveys (HCON-1 and HCON-2, the area was not observed during HCON-3), which were retrieved using the IRIS software; for SPIRE, we used the difference between two maps created combining four scans each; for *Planck*, we took the two *ringhalf* maps provided within the 2013 data release. The error is rather uniform across the HeViCS footprint and amounts to 0.03, 0.05, 0.05, 0.025, 0.015, 0.02, 0.03, and 0.035 MJy sr^{-1} for the IRAS 60 and 100 μm, SPIRE 250, 350, and 500 μm, *Planck* 350, 550, and 850 μm bands, respectively.

The instrumental uncertainty on the H I column density was directly estimated from the convolved ALFALFA maps, measuring the standard deviation of the featureless regions (fields V3 and V4) in the IVC map range, which is 1.0×10^{18} cm^{-2} for both the IVC and LVC channels. For the typical emissivities found here, the contribution of instrumental noise in H I column density maps is smaller than that from FIR/submm images (reaching a maximum of 0.005 MJy sr^{-1} in the 350 μm bands).

In all the dust emission maps we used, monochromatic flux densities were derived from wide band measurements assuming a flat spectrum, $F_\nu \propto 1/\nu$. We estimated color corrections assuming the average SED reconstructed using Eq. (1) as the *true* spectrum. They were found to be small, within less than 2% for most bands with the exception of the *Planck* 550 μm and 850 μm bands. In the following, we only correct the results obtained on these bands, by multiplying them by a factor 0.9. A similar result can be obtained using the *Planck* color correction software (Planck Collaboration IX 2014) and assuming the *Planck* MBB fit to high-latitude Galactic emission ($T = 20.3$ K, $\beta = 1.59$; Planck Collaboration XI 2014).

4. Results

In Table 1 we provide the parameters derived by fitting Eq. (1) to each image of dust emission for each field together with the errors estimated from the Monte Carlo analysis. The dust emission associated with LVC gas is estimated at a significant level in all fields and bands ($\epsilon_\nu^{\rm LVC} > 3\sigma$). In contrast, dust associated with IVC gas is significantly detected only in fields V1 and V2, while in fields V3 and V4 it is $\epsilon_\nu^{\rm IVC} < 3\sigma$ in most cases (the only exceptions are the marginal detections in the two IRAS bands for V4). This was not unexpected, given the low column density of IVC gas in the two southermost fields already shown in Fig. 3.

In Figs. 4 and 5 we show the pixel-by-pixel correlation between dust emission in the IRAS, SPIRE, and *Planck*-HFI 850 μm bands and column density of the two H I components for fields V1,V2 and V3,V4, respectively. For each velocity channel, the surface brightness is corrected by subtracting the fitted contribution from the other velocity channel and the offset and ecliptic latitude gradient. Thus, for the LVC gas, the surface brightness on the y-axis is $I_\nu - \epsilon_\nu^{\rm IVC} \times N_{\rm H\,I}^{\rm IVC} - O_\nu - E_\nu \times (b - b_0)$. The line and filled contours show the density of pixels before and after masking the regions that are deviant from the model by more than $3\sigma_{\rm R}$ at 250 μm; the dashed and solid straight lines are the fitted correlation in the two cases and the slope of the solid line is one of the ϵ_ν values reported in Table 1. In some cases, masking removes regions with high gas column density where significant excess emission shows up as an upturn of the contour plots

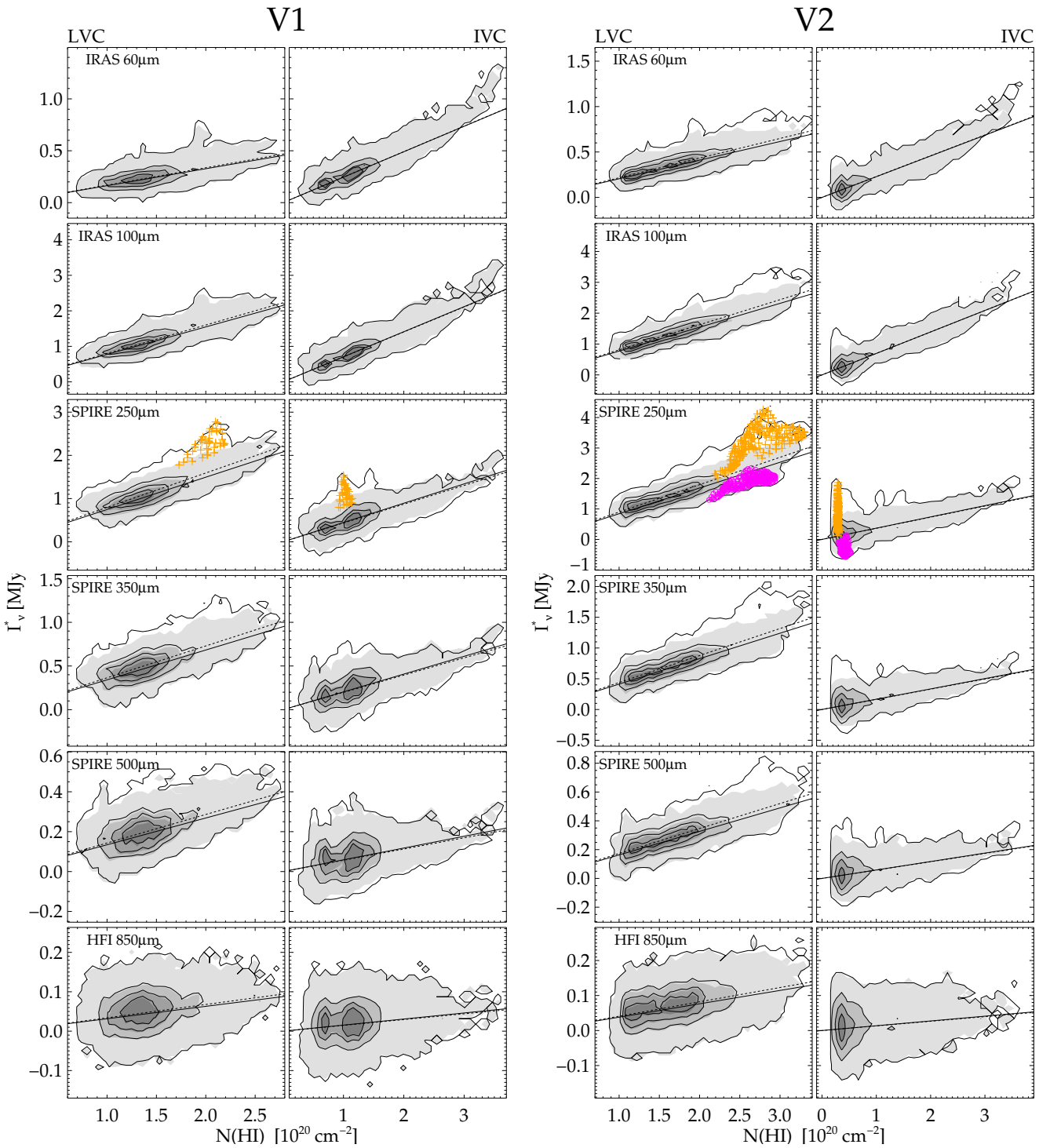

Fig. 4. Pixel-by-pixel correlation between dust emission and atomic gas column density for field V1 and V2 in the IRAS, SPIRE, and *Planck*-HFI 850 μm bands. For the LVC (IVC) gas component, the dust surface brightness I^*_ν is corrected to exclude the fitted contribution of the IVC (LVC) component; also, the offset and ecliptic latitude component is removed. Contours of constant pixel density enclosing 99.9, 75, 50, and 25% of the pixels are plotted. The gray-scale filled contours show the same correlation after masking regions that are deviant from the model by more than $3\sigma_R$ at 250 μm. Solid and dashed lines show the fitted correlation before and after the masking, respectively. Small changes in the fitted O_ν before and after the masking result in slight displacements of the line and filled contours. Orange crosses in the 250 μm panels refer to pixels within the isophotal ellipses of object 6 (in V1) and 14 (in V2). Magenta circles in the V2 250 μm panels show the region "N" of negative residuals (see Sect. 6 for details).

(see, e.g., the case for the LVC component at 250 μm in V2); in others, it affects regions at lower column density. The possible nature of these residuals is discussed in Sect. 6. In any case, the effect of masking on the parameter derivation is marginal: the emissivities derived without masking would be higher by up to a maximum of 1.5σ (for the LVC component in fields V2 and V3 at 100 and 250 μm), with σ the uncertainty estimated from the Monte Carlo analysis. Nevertheless, Table 1 reports the values

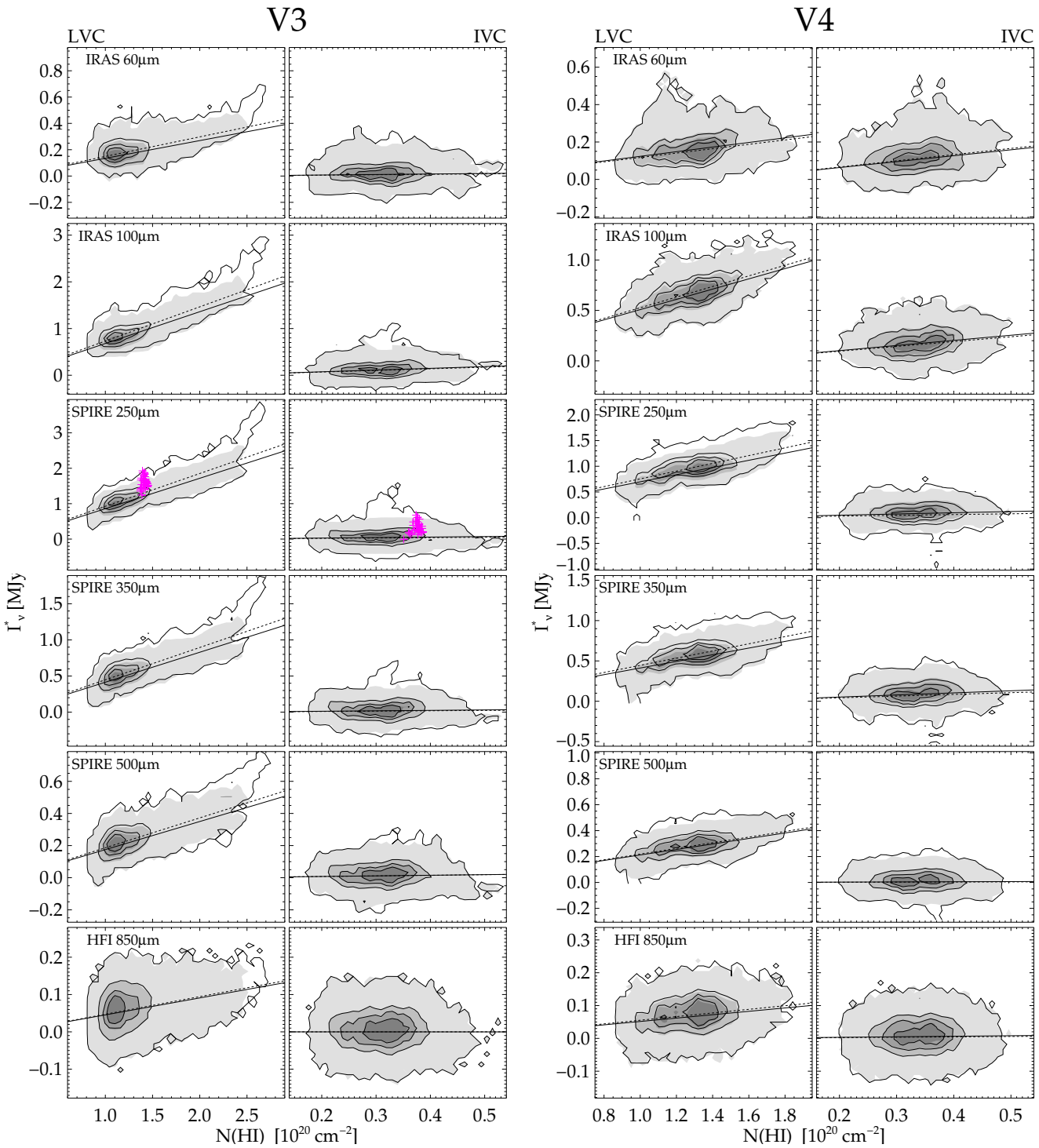

Fig. 5. Same as Fig. 4, but for field V3 and V4. Magenta crosses in the V3 250 μm panels show the pixels of region "G" (the galaxy VCC975; see Sect. 6.1 for details).

obtained after masking. The standard deviation of the residuals σ_R is also reported in the table, together with σ_C, which is derived by removing from σ_R the contribution of instrumental noise in dust emission and gas column density observation. The value σ_C includes all deviations from the adopted model and should be dominated, for the low column density regions, by the fluctuations in the CIB (Planck Collaboration XXIV 2011). Our estimates for σ_R (and σ_C) are very close to those obtained at 100 μm and in the *Planck* bands for low column density regions by Planck Collaboration XI (2014; see the first line in their Table C.1); they indeed confirm that the standard deviation of the residuals is dominated by the CIB fluctuations at all bands with the exception of 850 μm, where the contribution of instrumental noise is larger.

In the rest of this text, we focus our attention on the results obtained for the dust emissivities associated with the two gas components, $\epsilon_\nu^{\rm LVC}$ and $\epsilon_\nu^{\rm IVC}$; the discussion of the fitted offsets O_ν and ecliptic latitude gradients E_ν is presented in Appendix A. Figure 6 shows the emissivity SED derived for each HeViCS field. The mean emissivities for the full HeViCS coverage are

Table 1. Dust emissivities $\epsilon_\nu^{\rm LVC}$ and $\epsilon_\nu^{\rm IVC}$ for the two H I components, offsets O_ν and ecliptic latitude gradients E_ν, derived for each field and band considered in this work.

		IRAS		*Herschel*-SPIRE			*Planck*-HFI		
	Field	60 μm	100 μm	250 μm	350 μm	500 μm	350 μm	550 μm	850 μm
$\epsilon_\nu^{\rm LVC}$	V1	0.163 ± 0.012	0.774 ± 0.041	0.747 ± 0.045	0.341 ± 0.034	0.134 ± 0.024	0.399 ± 0.028	0.101 ± 0.012	0.0284 ± 0.0016
	V2	0.2051 ± 0.0089	0.773 ± 0.029	0.844 ± 0.037	0.414 ± 0.021	0.163 ± 0.011	0.462 ± 0.023	0.1288 ± 0.0066	0.03434 ± 0.00089
10^{-20} MJy sr^{-1} cm^2	V3	0.135 ± 0.014	0.680 ± 0.034	0.859 ± 0.039	0.415 ± 0.025	0.175 ± 0.011	0.484 ± 0.026	0.1495 ± 0.0098	0.0409 ± 0.0015
	V4	0.123 ± 0.025	0.508 ± 0.047	0.698 ± 0.061	0.412 ± 0.037	0.212 ± 0.022	0.486 ± 0.048	0.154 ± 0.019	0.0464 ± 0.0026
	avg.	0.157 ± 0.036	0.68 ± 0.12	0.787 ± 0.077	0.395 ± 0.036	0.171 ± 0.032	0.458 ± 0.041	0.133 ± 0.024	0.0375 ± 0.0078
$\epsilon_\nu^{\rm IVC}$	V1	0.245 ± 0.011	0.706 ± 0.029	0.447 ± 0.027	0.204 ± 0.022	0.059 ± 0.014	0.209 ± 0.020	0.0500 ± 0.0079	0.0139 ± 0.0012
	V2	0.228 ± 0.010	0.696 ± 0.027	0.370 ± 0.031	0.168 ± 0.020	0.0586 ± 0.0097	0.189 ± 0.022	0.0479 ± 0.0074	0.0123 ± 0.0012
10^{-20} MJy sr^{-1} cm^2	V3	*0.038 ± 0.071*	*0.37 ± 0.19*	*0.14 ± 0.19*	*0.06 ± 0.13*	*0.038 ± 0.057*	*-0.03 ± 0.12*	*-0.023 ± 0.049*	*-0.0002 ± 0.0073*
	V4	0.317 ± 0.066	0.51 ± 0.13	*0.24 ± 0.23*	*0.26 ± 0.13*	*0.013 ± 0.073*	*0.13 ± 0.17*	*0.049 ± 0.059*	*0.0145 ± 0.0093*
	avg.	0.263 ± 0.047	0.64 ± 0.11	0.408 ± 0.054	0.186 ± 0.026	0.05880 ± 0.00023	0.199 ± 0.014	0.0489 ± 0.0015	0.0131 ± 0.0011
O_ν	V1	0.201 ± 0.021	0.989 ± 0.063	-1.529 ± 0.064	-0.695 ± 0.047	-0.248 ± 0.031	0.238 ± 0.038	0.181 ± 0.016	0.0955 ± 0.0020
	V2	0.185 ± 0.018	1.051 ± 0.056	-1.677 ± 0.072	-0.811 ± 0.040	-0.314 ± 0.021	*0.105 ± 0.044*	0.113 ± 0.013	0.0811 ± 0.0019
MJy sr^{-1}	V3	0.231 ± 0.026	1.220 ± 0.054	-1.101 ± 0.068	-0.531 ± 0.043	-0.226 ± 0.017	0.188 ± 0.046	0.124 ± 0.016	0.0784 ± 0.0024
	V4	0.120 ± 0.033	1.303 ± 0.071	-0.97 ± 0.11	-0.619 ± 0.065	-0.286 ± 0.035	*0.146 ± 0.079*	0.101 ± 0.029	0.0667 ± 0.0043
E_ν	V1	-0.0206 ± 0.0036	-0.062 ± 0.011	*0.029 ± 0.011*	0.0303 ± 0.0091	*0.0135 ± 0.0060*	0.0472 ± 0.0068	0.0228 ± 0.0029	0.00909 ± 0.00033
	V2	*-0.0021 ± 0.0039*	*-0.0006 ± 0.0096*	*-0.012 ± 0.012*	*-0.0116 ± 0.0079*	*-0.0042 ± 0.0044*	*0.0104 ± 0.0091*	*0.0009 ± 0.0033*	*0.00051 ± 0.00045*
MJy sr^{-1} deg^{-1}	V3	0.0769 ± 0.0034	0.0475 ± 0.0080	-0.0729 ± 0.0089	-0.0370 ± 0.0055	-0.0158 ± 0.0022	-0.0231 ± 0.0056	-0.0077 ± 0.0019	*-0.00075 ± 0.00027*
	V4	-0.0802 ± 0.0042	*-0.0139 ± 0.0056*	*0.0154 ± 0.0077*	*0.0113 ± 0.0046*	*0.0081 ± 0.0031*	0.0230 ± 0.0062	*0.0066 ± 0.0025*	0.00172 ± 0.00035
$\sigma_{\rm R}(\sigma_{\rm C})$	V1	0.048 (0.037)	0.11 (0.10)	0.14 (0.13)	0.10 (0.10)	0.061 (0.059)	0.10 (0.099)	0.057 (0.048)	0.037 (0.012)
	V2	0.049 (0.039)	0.13 (0.12)	0.16 (0.15)	0.096 (0.093)	0.054 (0.052)	0.11 (0.10)	0.057 (0.048)	0.037 (0.012)
MJy sr^{-1}	V3	0.047 (0.036)	0.097 (0.083)	0.12 (0.11)	0.087 (0.083)	0.050 (0.048)	0.093 (0.091)	0.057 (0.048)	0.037 (0.012)
	V4	0.045 (0.033)	0.088 (0.072)	0.11 (0.10)	0.083 (0.079)	0.050 (0.048)	0.091 (0.089)	0.054 (0.045)	0.037 (0.012)

Notes. Errors are derived with the Monte Carlo technique described in Sect. 3. Estimates below 3σ are in italics. $\sigma_{\rm R}$ is the standard deviation of the residuals R_ν. $\sigma_{\rm C}$ is derived from $\sigma_{\rm R}$ after removing the contribution to the uncertainties due to instrumental noise in dust emission and H I maps. For $\epsilon_\nu^{\rm LVC}$ and $\epsilon_\nu^{\rm IVC}$, the average over the fields is also reported (excluding low *S/N* values) together with its standard deviation.

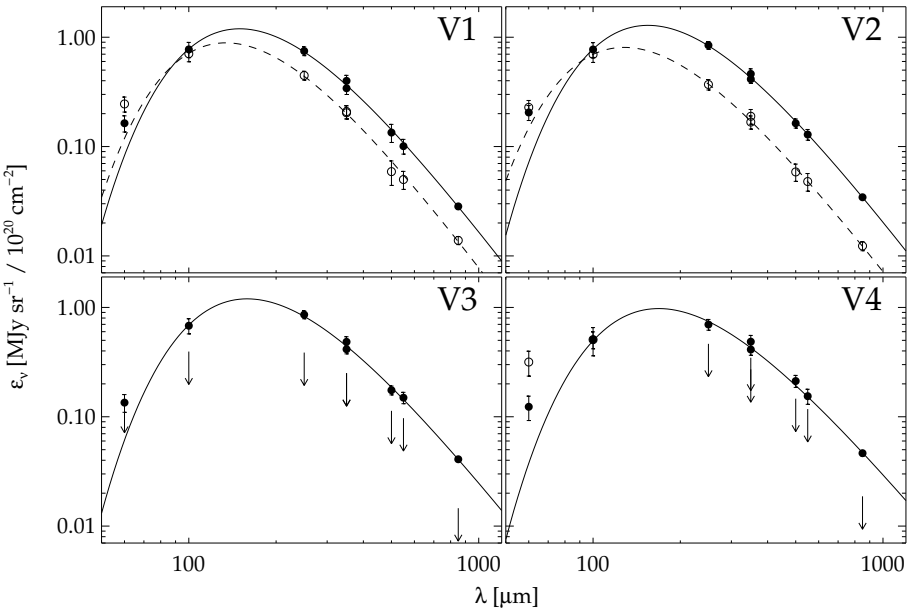

Fig. 6. Emissivities for the four HeViCS fields. Filled symbols and solid lines refer to the estimates for $\epsilon_\nu^{\rm LVC}$ and their (variable β) MBB fits, respectively; open symbols, 2σ upper limits and dashed lines refer to $\epsilon^{\rm IVC}$.

shown in Fig. 7 and reported in Table 1. The scatter, as measured by the standard deviation of the emissivities of the various field, is relatively small, and generally is below 15–20% of the mean value. This is however larger than the individual uncertainties of each estimate (typically in the range ~5–10%), pointing to real field-to-field variations in the emissivity values (see next section).

It is important to remember that, in order to compare our results with those in Planck Collaboration XI (2014), we scaled our ALFALFA map to match the LAB column densities (Sect. 2.1). If we had not scaled our map, the derived emissivities would have been lower by 6% for the LVC component; this is a difference that is compatible with the estimated uncertainties in the emissivity derivation, corresponding to a maximum of 1.5σ at 100 μm, and by a larger amount, 14%, for the IVC component (equivalent to a maximum of 3.5σ at 100 μm). These differences are entirely due to the gain correction described in Sect. 2.1, since the offset between ALFALFA and LAB is negligible.

We found the SPIRE and *Planck* emissivities in the overlapping band at 350 μm to be marginally consistent, with a difference of about 1.5σ for the LVC component; the 350 μm SPIRE/*Planck* emissivity ratio is 0.86, which is entirely due to the relative gain of the SPIRE and *Planck* maps used in this work. Instead, the accurate analysis of Bertincourt et al. (2016) finds that the relative gain is close to unity. The difference cannot be accounted for by including color corrections (which we neglected at 350 μm), nor by switching to the most recent releases of *Planck* and *Herschel* data. The use of the latest pipeline-reduced SPIRE 350 μm (downloaded from the Herschel Science Archive in August 2016) confirms our result. The reason for the difference is unknown. We are tempted to impute it to the peculiarities of the HeViCS fields. In fact, the HeViCS average surface brightness is at least a factor two smaller than that of the *Spider cirrus* molecular cloud, which is the lowest intensity field used by Bertincourt et al. (2016). When our procedures for data manipulation and analysis are applied to pipeline-reduced SPIRE data of that target, we indeed obtain a result that is entirely consistent with their findings.

5. Absorption cross sections of high-latitude dust

The SED of diffuse high-latitude dust is one of the test beds for Galactic dust models because of two simplifying conditions: dust emission can be reasonably assumed to be optically thin in the diffuse medium; and the line of sight at high latitude crosses a very limited range of dust environments, and hence, a single heating source can be assumed, that provided by the LISRF.

A very simple description of dust emission is provided by a MBB. Assuming that all dust grains share the same composition and size (and thus attain the same temperature T under the same heating conditions), the emissivity SED can be written as

$$\epsilon_\nu = \frac{\tau_\nu}{N_{\rm H}} B_\nu(T).$$

The FIR/submm absorption cross section (per unit hydrogen atom) is usually described by a power law; adopting 250 μm as the reference wavelength, it can be written as

$$\frac{\tau_\nu}{N_{\rm H}} = \frac{\tau(250\,\mu{\rm m})}{N_{\rm H}} \times (250\,\mu{\rm m}/\lambda)^\beta.$$

A fit to the emissivity SEDs can thus retrieve the dust temperature T and the absorption cross section normalization $\tau(250\,\mu{\rm m})/N_{\rm H}$ and spectral index β.

In general, a MBB results in an adequate fit to the observations, provided that data points contaminated by dust at hotter temperatures or not emitting at thermal equilibrium are excluded from the analysis; for this reason, the 60 μm emissivities are not included in the fits presented here. However, the parameters retrieved from the fits might be different from those of the underlying dust population. In particular, simultaneous solutions for T and β might be degenerate, since both quantities determine the SED shape. An inverse correlation between these parameters is generally found and imputed to a bias due to standard χ^2 minimization techniques, calling for more sophisticated Bayesian-fitting methods for a rigorous treatment of all involved uncertainties (see, e.g., Kelly et al. 2012), or to line-of-sight temperature mixing, even at high Galactic latitude (see, e.g., Veneziani et al. 2010; Bracco et al. 2011). Even when dust is heated by a single radiation field, grains attain different temperatures, depending on their size and composition. This temperature distribution broadens the SED and biases the observed β to values lower than the intrinsic spectral index of dust, in particular for radiation fields that are weaker than the LISRF (Hunt et al. 2015).

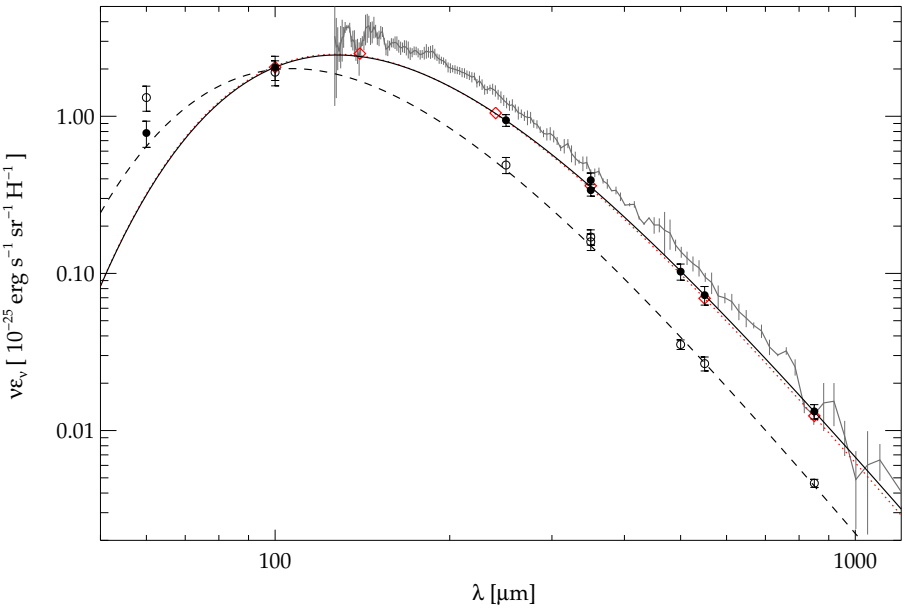

Fig. 7. Mean emissivities for the full HeViCS coverage. Filled circles and solid lines refer to the estimates for $\epsilon^{\rm LVC}$ and their (variable β) MBB fits, respectively; open circles and dashed lines refer to $\epsilon^{\rm IVC}$. The error bars show the standard deviation of the mean. The red squares are the COBE-DIRBE and *Planck*-HFI emissivities derived in the southern Galactic pole (Planck Collaboration Int. XVII 2014); the red dotted line is the fit to *Planck* high-latitude emissivities (Planck Collaboration XI 2014); the gray line and error bars refer to the high-latitude emissivities from FIRAS (Compiègne et al. 2011).

Table 2. Parameters of single temperature MBB fits to the emissivity SEDs.

	V1	V2	V3	V4	Avg.
			LVC		
$\frac{\tau(250\ \mu{\rm m})}{N{\rm H\,I}}/\frac{10^{-25}\ {\rm cm}^2}{\rm H}$	0.44 ± 0.11	0.54 ± 0.12	0.52 ± 0.11	0.49 ± 0.13	0.49 ± 0.13
T/K	20.7 ± 1.4	20.1 ± 1.2	20.3 ± 1.2	20.0 ± 1.4	20.4 ± 1.5
β	1.69 ± 0.14	1.67 ± 0.11	1.51 ± 0.12	1.33 ± 0.14	1.53 ± 0.17
$\frac{\tau(250\ \mu{\rm m})}{N{\rm H\,I}}/\frac{10^{-25}\ {\rm cm}^2}{\rm H}$	0.370 ± 0.030	0.467 ± 0.023	0.596 ± 0.038	0.755 ± 0.072	0.525 ± 0.052
T/K	21.6 ± 1.1	20.92 ± 0.50	19.61 ± 0.52	17.91 ± 0.68	20.00 ± 0.70
β			1.59 (fixed)		
			IVC		
$\frac{\tau(250\ \mu{\rm m})}{N{\rm H\,I}}/\frac{10^{-25}\ {\rm cm}^2}{\rm H}$	0.200 ± 0.056	0.139 ± 0.043	–	–	0.150 ± 0.040
T/K	22.7 ± 1.9	24.5 ± 2.3	–	–	23.9 ± 2.0
β	1.77 ± 0.16	1.63 ± 0.18	–	–	1.65 ± 0.15
$\frac{\tau(250\ \mu{\rm m})}{N{\rm H\,I}}/\frac{10^{-25}\ {\rm cm}^2}{\rm H}$	0.153 ± 0.015	0.130 ± 0.014	–	–	0.137 ± 0.011
T/K	24.7 ± 1.6	25.1 ± 1.2	–	–	24.6 ± 1.2
β			1.59 (fixed)		

For the sake of simplicity, and in analogy to Planck Collaboration XXIV (2011) and Planck Collaboration XI (2014), we adopt here a single MBB model and fit it to the data for each field, and to the average emissivity, using a standard χ^2 minimization routine (`mpfit` for IDL; Markwardt 2009); we allow β to vary (these fits are plotted in Figs. 6 and 7) but we also produce fits using a fixed β. The parameters derived from the fits are given in Table 2.

5.1. Low velocity cloud dust

For dust associated with LVC gas, we find a trend of relatively higher emissivities at longer wavelengths in the two southernmost fields. This translates to fits with spectral indices increasing from $\beta \approx 1.3$ in field V4 to $\beta \approx 1.7$ in field V1. Instead, the temperature is relatively constant in the four fields ($T = 20.0$–20.7 K). If instead $\beta = 1.59$ is used, as derived by Planck Collaboration XI (2014) on the diffuse high Galactic latitude medium (DHGL; defined by $b > 15°$, $N_{\rm H\,I} < 5 \times 10^{20}$ cm^{-2}; Compiègne et al. 2011), the fitted temperature reduces to 17.9 K in field V4 and increases to 21.6K in field V1. This behavior is a clear effect of the T-β degeneracy (Shetty et al. 2009).

The fit to the average emissivities, as well as the emissivities themselves, is consistent with the previous fit to the DHGL medium (red dotted line in Fig. 7). For a variable β, we find $\tau(250\,\mu{\rm m})/N_{\rm H} = (0.49 \pm 0.13) \times 10^{-25}$ cm^2 H^{-1}, $T = 20.4 \pm 1.5$ K and $\beta = 1.53 \pm 0.17$, while the Planck Collaboration XI (2014) values for the DHGL are $\tau(250\ \mu{\rm m})/N_{\rm H} = (0.49 \pm 0.14) \times 10^{-25}$ cm^2 H^{-1}, $T = 20.3 \pm 1.3$ K and $\beta = 1.59 \pm 0.12$. Analogous consistency is obtained by fitting the COBE-DIRBE and *Planck*-HFI emissivities of the south Galactic pole (red diamonds in Fig. 7; Planck Collaboration Int. XVII 2014): $\tau(250\ \mu{\rm m})/N_{\rm H} = (0.55 \pm 0.05) \times 10^{-25}$ cm^2 H^{-1}, $T = 19.8 \pm 1.0$ K and $\beta = 1.65 \pm 0.10$. The emissivities derived in this work are thus

representative of the average properties of high-latitude dust. This is remarkable, since the DHGL and the south Galactic pole medium cover 50% and 20% of the sky, respectively, while our fields are just ~0.2%.

5.2. Implications for dust modeling

The *Herschel*-SPIRE emissivities derived in this work also share with *Planck*-HFI the inconsistency with the dust emission spectra obtained by the FIRAS instrument aboard the COBE satellite. The HFI team switched from a FIRAS- to a planet- (Uranus and Neptune) based calibration for the 350 μm and 550 μm bands, after recognizing a bias of uncertain origin in the FIRAS data (Planck Collaboration VIII 2014). The FIRAS emissivity spectrum for the DHGL derived by Compiègne et al. (2011) is shown in Fig. 7. As it has been pointed out, the new emissivities, confirmed here by the analysis of (Neptune-calibrated) SPIRE data, ask for a revision of the current models for MW dust, whose properties (grain composition and size distribution) were adjusted to reproduce the FIRAS spectrum (Planck Collaboration Int. XVII 2014; Planck Collaboration Int. XXIX 2016). For example, the MC10 dust model distributed with the `DustEM` software (Compiègne et al. 2011) reproduced the FIRAS DHGL emissivities when heated by the LISRF, after correcting these emissivities, mostly for the contribution of ionized gas to the hydrogen column density, with a small correction for molecular gas. Using the new emissivities, the absorption cross sections would need to be adjusted so that emission at, for example, 250 μm, is lower by 20%, as the modeled SED shape for LISRF heating is still consistent with the observations (Planck Collaboration Int. XVII 2014). If instead the new estimate of the LISRF proposed by Draine (2011) is adopted, new dust models should decrease their FIR output by 30% with respect to FIRAS.

In Appendix B we discuss the implications of these new absorption cross sections in the determination of the dust masses of external galaxies.

5.3. IVC dust

Dust associated with IVC is found to have a lower emissivity than LVC dust (on average by about 1/2 at 250 μm) and a lower absorption cross section. This result confirms the findings of Planck Collaboration XXIV (2011), which tentatively impute the different properties of IVC dust to a larger amount of smaller grains not emitting at thermal equilibrium. Dust processing leading to smaller grain sizes (in particular grain shattering, dominant over gas-grain sputtering; Bocchio et al. 2014) is indeed expected in the shocked gas of Galactic fountains, which has been proposed as an explanation for the IVC medium (for a review, see Wakker & van Woerden 1997). A lower opacity cross section and a higher temperature is found for the IVC medium than for LVC dust for relatively similar β values. Assuming $\beta = 1.59$, the emissivity is $\tau(250\,\mu\mathrm{m})/N_\mathrm{H} = (0.14 \pm 0.01) \times 10^{-25}$ cm^2 H^{-1} with $T \approx 25$ K. Unfortunately, we cannot quantitatively compare our results with those obtained on LVC and IVC dust by Planck Collaboration XXIV (2011), since they used an earlier release of *Planck* data calibrated on FIRAS, and adopted the older FIRAS-based value $\beta = 1.8$ for both dust components. We only note that the SED is *bluer* because of the different dust properties, rather than because of a heating source more intense than the LISRF, as the IVC medium is located higher above the Galactic plane than the LVC (Sect. 2.1).

6. Residuals

In Fig. 8 we show the observed dust emission, the dust emission modeled from the H I observations using the derived emissivities (Eq. (1)), and the residuals in the SPIRE 250 μm band. In order to show observations and models on the same scale, the large-scale terms derived from the fit (offsets and ecliptic latitude gradients) have been subtracted from the images. For ease of presentations, the four HeViCS fields are combined in a single image by removing the small residual offsets between the fields (see Appendix A); the analysis, however, was conducted separately on each field, as detailed in the previous sections. Analogous figures for the other IRAS, SPIRE, and HFI bands are shown in Appendix C.

Models and residuals show consistent results in all bands. The 60 μm residuals (Fig. C.1) are similar to those at 100 μm (Fig. C.2), both IRAS bands having a similar contribution from dust associated with LVC and IVC gas (at least in the V1 and V2 areas). All SPIRE and HFI bands between 250 μm and 850 μm (Figs. 8, C.3 to C.7), where the LVC gas contribution to dust emission is at least twice that of IVC, show basically the same pattern in observations, models, and residuals; the largest deviations from the models, however, more easily stand out in shorter wavelength bands, where they dominate over the background noise.

A visual comparison between data and models shows that, on large scales, there is a good correspondence between the features seen in dust and H I emission. We have already shown the good correlation between these two ISM tracers in Sect. 4. However, there are significative deviations at smaller scales: infrared emission appears less filamentary than H I, mostly because of the superimposition of the clumpier CIB to the cirrus; (some) regions of high H I column density have infrared emission much in excess of those predicted by the model.

6.1. A catalog of excess regions

We have identified the main excess regions by running the source extraction software `sextractor` (Bertin & Arnouts 1996) on the 250 μm residual maps. We selected all sources with pixel values above $3\sigma_\mathrm{R}$ and with size larger than a beam (about 12 pixels).

To avoid fragmentation, the mask of bright background sources was unset. An initial source list was produced and pruned of those objects whose isophotal ellipses included a significant contribution from background objects, both masked and unmasked. In fact, about half of the Virgo cluster galaxies detected by Auld et al. (2013) were not masked. The brightest is VCC975 with a flux of 1.1 Jy at 250 μm. It is shown with the magenta circle marked with "G" in Fig. 8; the corresponding pixels are plotted as crosses on the 250 μm V3 panels in Fig. 5. Even for the brightest unmasked source the contribution to the emissivity determination is limited: only pixels on the peak of the galaxy have been excluded from the fit.

The contribution from the background sources was estimated by making mock images of the extragalactic objects, including the Virgo cluster galaxies detected at 250 μm by Auld et al. (2013) and the objects in the HeViCS SPIRE point source catalog of Pappalardo et al. (2015); we assume, for simplicity, that all objects can be described by point sources at the adopted resolution. The few tens of thousands point sources of Pappalardo et al. (2015) produce, when smoothed to the adopted resolution, a map characterized by fluctuations over an average background. We estimated values of 0.106 ± 0.041, 0.074 ± 0.033 and 0.027 ± 0.020 MJy sr^{-1} for the average background and fluctuations at 250, 350, and 500 μm via histogram fitting. When

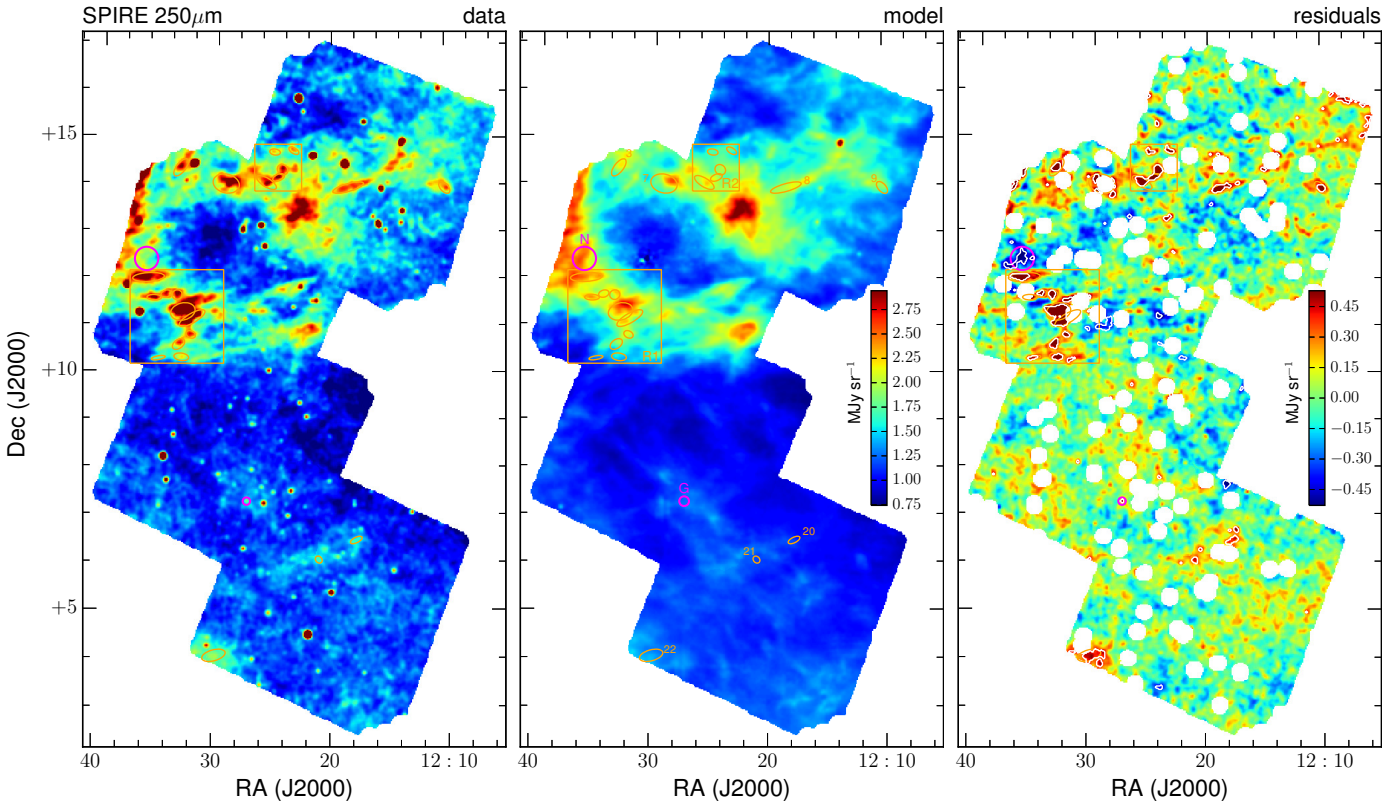

Fig. 8. Observations (*left column*), models (*middle column*), and residuals (*right column*) of the HeViCS field in the SPIRE 250 μm band. Observations and models were subtracted by the large-scale terms $O_\nu + E_\nu \times (b - b_0)$ and are shown on the same color scale. The color scale of the residuals goes from -4 to $4\sigma_R$ (Table 1); round white areas show the object mask applied before the fitting, while white contours encircle the regions where residuals are larger than $3\sigma_R$ (excluded during the fitting). The orange numbered ellipses and square regions refer to the high positive residual regions listed in Table 3 and shown in Fig. 9. The magenta circle labeled "N" highlights a region with high negative residuals; the magenta circle labeled "G" is centered on an unmasked Virgo cluster galaxy.

compared to estimates of the CIB (Gispert et al. 2000), these average values show that detected point sources contribute to only a fraction of it (up to 15% at 250 μm; see also Béthermin et al. 2012). Also, the background fluctuations inferred from resolved sources are smaller than the σ_C values found in this work (Table 1), which are mostly due to undetected sources, together with the large residuals from the foreground cirrus modeling. When estimating the contribution of point sources to the excess regions, we neglected the average value, which should be accounted for in the constant offsets O_ν.

To keep contamination low, we only retained objects where the contribution from galaxies was smaller than 20% the total residual. The final catalog is shown in Table 3, where for each object we list the center, semi-major axis, axis ratio, and position angle of the major axis of the isophotal ellipses together with the median and peak residuals within the isophote. The remaining columns are described in the following. Isophotal ellipses are shown in the maps of Fig. 8. Individual objects or group of objects are also shown in Fig. 9, overlayed on the 250 μm map at the original resolution ($FWHM \approx 18''$), providing a better view of the morphology of diffuse emission.

6.2. A few examples

A large group of high residual regions is present in the V2 tile, near (and partly in correspondence with) the overlap with V3 (we define this region R1 in Figs. 8 and 9). This region consists of several clouds interconnected by a filamentary structure. The object with the largest residual is # 14 of Table 3. The pixels within its isophotal ellipse are shown as crosses in the 250 μm dust-H I correlation panels for V2 (Fig. 4). The excess is clearly associated with the higher column density LVC gas, appearing as excess emission for the lowest density IVC gas in the field. However, the region does not lay exactly on the local LVC peak (the maximum being at the edge of the ellipse, as shown in the middle panel of Fig. 8). Similar excesses have been found in a recent work by Reach et al. (2015), who study the correlation between H I column density from the Arecibo GALFA survey and dust emission from *Planck*. Our work is analogous to theirs, although the column densities of the HeViCS fields are smaller than those of the high-latitude clouds studied by Reach et al. (2015). They argue that the residuals could be produced by different local dust properties; a local increase of the ISM density that is not traced by N_{HI} due to the presence of molecular gas; and an underestimation of N_H due to the neglect of H I self-absorption. We examine these alternatives below.

6.2.1. Different dust properties

If one assumes that the LVC H I column density is a faithful tracer of the full ISM density, the pixel-by-pixel correlation of the excess emission could be explained by the contribution of dust at higher emissivity than that for the diffuse medium. However, it is not straightforward to derive the increase in emissivity without knowing the amount of the total gas column density that is associated with the more emissive dust. If the whole column

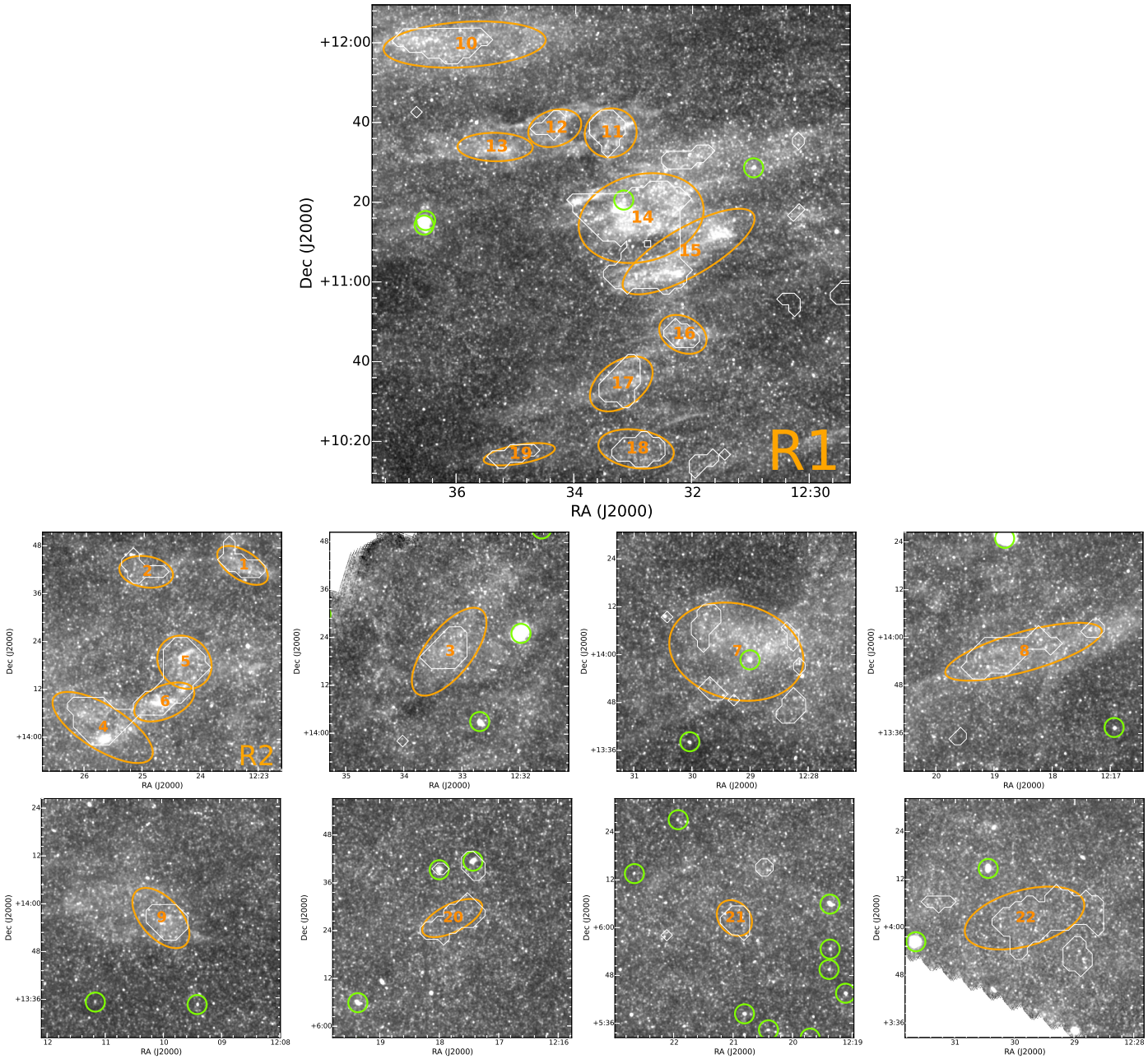

Fig. 9. Regions with high positive residuals, superimposed on the SPIRE 250 μm map at the original resolution. For each object detected by `sextractor`, isophotal ellipses are shown (see Table 3). White contours correspond to regions masked during the emissivity determination. Green circles (diameter = 2 *FWHM*) show the VCC galaxies detected by Auld et al. (2013). The size of the R1 panel is $2^\circ \times 2^\circ$, $1^\circ \times 1^\circ$ for all the others.

density under the excess area is associated with dust at a higher emissivity $\epsilon_\nu^{\rm LVC}|_{\rm ex}$, the residuals can be written as the difference between the emission of this dust and the emission that is predicted from the whole field,

$$R_\nu = \epsilon_\nu^{\rm LVC}|_{\rm ex} N_{\rm HI} - \epsilon_\nu^{\rm LVC} N_{\rm HI},$$

which leads to

$$\frac{\epsilon_\nu^{\rm LVC}\big|_{\rm ex}}{\epsilon_\nu^{\rm LVC}} = 1 + \frac{R_\nu}{\epsilon_\nu^{\rm LVC} N_{\rm HI}}.$$

At 250 μm, the excess area has residuals values $R_\nu = 0.77$ and 1.8 MJy sr^{-1} for the average and for the peak, respectively, which would correspond to a moderate increase in emissivity by a factor of 1.3 to 1.8. In principle, this higher emissivity can be simply due to a larger dust temperature in the excess region with respect to the average temperature derived from the full field. However, the SED of the residuals within the area is consistent with a temperature that is close to the average temperature of the field ($T = 20.4$ K for $\beta = 1.59$, to be compared with $T = 20.9 \pm 0.5$ for field V2; see Fig. 10).

For the same temperature, a higher emissivity corresponds to a higher dust absorption cross section. Larger dust cross sections are found in dense Milky Way clouds. For example, Juvela et al. (2015) measured the absorption cross sections in Galactic cold cores using *Planck* and *Herschel* data, finding values up to more than three times those of the diffuse medium. The larger cross section can result from grain growth due to accretion of gas atoms (C, H) into mantles (Ysard et al. 2015; Köhler et al. 2015), the formation of ice

Table 3. Excess regions at 250 μm.

	RA[°]	Dec [°]	a [′]	b/a	PA [°]	R_ν [MJy sr^{-1}]		$\epsilon_\nu^{\rm LVC}\big\vert_{\rm ex}/\epsilon_\nu^{\rm LVC}$		$N_{\rm H_2}$ [cm^{-2}]		τ	
						median	peak	median	peak	median	peak	median	peak
1	185.823746	14.725930	7.2	0.50	57	0.50	0.70	1.4	1.5	3.4e+19	4.7e+19	0.9	1.2
2	186.240067	14.695560	6.8	0.57	80	0.45	0.57	1.3	1.4	3.0e+19	3.8e+19	0.8	1.0
3	188.306244	14.343020	13.2	0.44	141	0.45	0.90	1.2	1.4	2.7e+19	5.3e+19	0.6	1.1
4	186.421265	14.043010	14.4	0.39	58	0.46	0.94	1.3	1.6	3.1e+19	6.3e+19	0.8	1.4
5	186.071487	14.318910	7.2	0.87	48	0.60	1.00	1.4	1.6	4.0e+19	6.7e+19	1.0	1.5
6	186.156967	14.151900	8.0	0.51	112	0.71	1.08	1.5	1.7	4.8e+19	7.2e+19	1.1	1.6
7	187.308731	14.012690	17.1	0.70	76	0.52	1.33	1.3	1.6	3.1e+19	7.9e+19	0.7	1.5
8	184.624084	13.942280	20.3	0.24	105	0.46	0.72	1.3	1.5	3.1e+19	4.8e+19	0.8	1.2
9	182.506973	13.937320	9.1	0.55	42	0.45	0.78	1.4	1.6	3.0e+19	5.2e+19	0.9	1.5
10	188.974243	11.995280	20.4	0.28	93	0.50	0.92	1.2	1.4	3.0e+19	5.4e+19	0.5	0.9
11	188.348526	11.628510	6.6	0.93	107	0.58	0.87	1.3	1.4	3.4e+19	5.1e+19	0.7	1.0
12	188.587433	11.647190	6.8	0.66	106	0.49	0.78	1.2	1.4	2.9e+19	4.6e+19	0.6	0.9
13	188.841675	11.567190	9.4	0.38	89	0.45	0.73	1.2	1.3	2.7e+19	4.3e+19	0.5	0.8
14	188.217331	11.272350	15.9	0.68	104	0.77	1.80	1.3	1.8	4.5e+19	1.1e+20	0.8	1.8
15	188.014572	11.132850	18.8	0.32	119	0.92	1.49	1.4	1.7	5.4e+19	8.8e+19	1.1	1.6
16	188.038177	10.786410	6.3	0.71	62	0.49	0.69	1.2	1.3	2.9e+19	4.1e+19	0.6	0.8
17	188.299667	10.578530	8.9	0.63	126	0.50	0.83	1.3	1.5	3.0e+19	4.9e+19	0.7	1.1
18	188.235886	10.306960	9.5	0.50	81	0.44	0.75	1.3	1.5	2.6e+19	4.5e+19	0.8	1.3
19	188.732086	10.282890	9.1	0.26	99	0.42	0.52	1.3	1.4	2.5e+19	3.1e+19	0.9	1.0
20	184.445099	6.452250	8.2	0.42	116	0.40	0.48	1.4	1.6	2.9e+19	3.4e+19	1.1	1.4
21	185.244553	6.040510	4.9	0.80	42	0.40	0.48	1.4	1.5	2.9e+19	3.4e+19	1.0	1.2
22	187.458755	4.039970	15.4	0.45	105	0.41	0.52	1.4	1.4	2.9e+19	3.7e+19	0.9	1.1

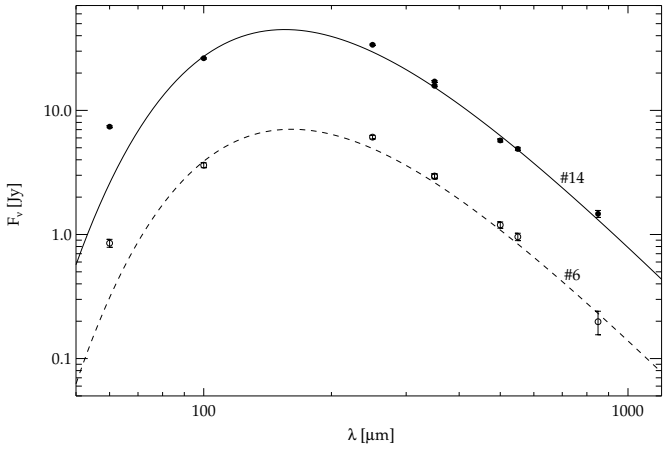

Fig. 10. Spectral energy distribution of object # 14 in field V2 and # 6 in V1. Error bars for each aperture have been estimated from $\sigma_{\rm R}$ (Table 1). Modified blackbody fits assume $\beta = 1.59$ and exclude the 60 μm data.

mantles, and the coagulation of grains (Ossenkopf & Henning 1994; Köhler et al. 2015). However, our excess regions lack the main characteristic defining dense Galactic cold clouds, i.e., the lower temperature with respect to the surrounding medium. Also, Galactic cold clumps have on average higher column densities (Planck Collaboration XXIII 2011); none of the sources of the *Planck* Catalogue of Galactic Cold Clumps (Planck Collaboration XXVIII 2016) falls within the HeViCS footprint.

6.2.2. Molecular gas

Conversely, if one assumes that the dust properties do not change significantly in the limited column density range of the HeViCS fields, the excess could be explained by untraced molecular gas. Indeed, excess emission over the dust/H I correlation has been used to detect molecular clouds (see, e.g., Desert et al. 1988; Reach et al. 1998). Because of the limited resolution of available surveys, these searches only detected larger excesses than those measured here. For instance, the region we are considering is marked by low surface brightness contours in the 100 μm excess map of the north Galactic pole in Reach et al. (1998) and was not included in their final catalog of detected clouds.

Adopting the same emissivity as for atomic gas, the residuals could be used to derive the column density of untraced H nucleons, and thus to estimate the H_2 column density,

$$N_{\rm H_2} = \frac{1}{2}\frac{R_\nu}{\epsilon_\nu^{\rm LVC}}.$$

For the average and peak column densities of LVC gas in the excess area one should expect a molecular gas column density ranging from $N_{\rm H_2} = 0.4$ to 1.1×10^{20} cm^{-2}. Unfortunately, there are no molecular gas surveys at high Galactic latitude that are sensitive enough to detect these column density levels. The HeViCS area has been covered by the North Galactic Hemisphere CO(1–0) survey of Hartmann et al. (1998), with a sparsely sampled $\sim 1^\circ \times 1^\circ$ grid. However, CO emission was not detected in any of the pointings with a 2σ upper limit corresponding to $N_{\rm H_2} = 1.2 \times 10^{20}$ cm^{-2} (assuming the typical velocity width of the clouds detected in the survey and the standard $X_{\rm CO} = 2 \times 10^{20}$ cm^{-2} (K km s^{-1})$^{-1}$ conversion factor for Galactic molecular clouds; Bolatto et al. 2013). Besides having a detection limit that is close to that inferred from our highest excess region, the grid of pointings (with beam $FWHM = 8\farcm4$) misses all regions with high residuals. The fully sampled CO(1–0) map derived from *Planck* observations cannot be of help either, as it is featureless within the HeViCS footprint (we used the type-3

map of Planck Collaboration XIII 2014); it also has a 2σ upper limit that is four times higher than that of Hartmann et al. (1998).

Gillmon & Shull (2006) studied the correlation between IRAS surface brightnesses and molecular gas column densities derived from UV absorption lines in a sample of high-latitude AGNs; they concluded that a significant amount of H_2 is present in most diffuse cirrus clouds. Unfortunately, the limited dynamic range of our residuals does not help us to understand if the excess regions are just the tip of diffuse molecular clouds or isolated cores ($3\sigma_R$ corresponding to about 0.3×10^{20} cm^{-2}, a third of the estimate for the peak value). Molecular gas with $N_{H_2} \approx 2{-}3 \times 10^{20}$ cm^{-2} was detected by Cortese et al. (2010) in correspondence to a 5′ plume to the north of the interacting pair NGC 4435/NGC 4438 and interpreted as a compact cirrus cloud; the plume is detected in HeViCS images, but it is masked in our analysis because of the proximity to the bright galaxies. Compact molecular clouds, called small area molecular structures (SAMS), with $N_{H_2} \lesssim 1 \times 10^{20}$ cm^{-2} have been found in a few limited fields at high Galactic latitude (Heithausen 2002, 2007). Dust emission associated with SAMS has been detected in SPIRE images (Heithausen 2012), and indeed for one of these structures dust emissivity in excess of that for the diffuse medium has been reported (Davies et al. 2010b). The SAMS studied so far are however smaller, with typical sizes of 1–2′, yet they tend to be grouped in clusters (Heithausen 2007). Thus, our excess region, which also appears more extended and filamentary at the original 250 μm resolution could be a web of connected SAMS. Heithausen (2002) claims that SAMS are transitory objects, as they are not sufficiently shielded from UV radiation to survive for a long time (Heithausen 2002, 2007). Yet, Gillmon & Shull (2006) found that H_2 self-shielding can already occur for $N_{H_2} \gtrsim 10^{18}$ cm^{-2} in regions with $I_\nu \gtrsim 2$ MJy sr^{-1} at 100 μm. These surface brightness levels are indeed consistent with those found here.

6.2.3. H I self-absorption

Instead, if the excess is due to the neglect of H I self-absorption in the estimate of the gas column density, the total H I column density should be 30% to 80% larger than what is actually measured in the optically thin limit for LVC gas; the estimate depends on the use of average or peak values, respectively. The optical depth at the line center would need to range between 0.8 and 1.8 to explain the excess (Eq. (15) in Reach et al. 2015). These optical depths are larger than those derived from H I absorption (see Sect. 2.1), yet none of the probed lines of sight falls on a high residual region. The values estimated here are smaller than those derived in the higher density regions analyzed by Reach et al. (2015); even if they are seldom encountered at high Galactic latitude (less than 4% of $b > 30°$ lines of sight in Heiles & Troland 2003, have higher optical depths) the coverage of the residuals makes this hypothesis compatible with the absorption line observations. However, it is not clear why the excess in object # 14 should be due to H I self-absorption, while the peak of N_{HI}^{LVC} (at the northern edge of the selected area) does not show a similarly high residual.

Summarizing, we have no reason to favor one of the proposed explanations for the excesses over the other. We are tempted to exclude H I self-absorption, because of the mismatch between high column densities and high optical depth estimates, and to favor the molecular gas explanation because of the detection of similar column densities in other fields. Also, the latter hypothesis could be more readily tested with future dedicated observations of molecular lines over the areas of the excess regions.

As another example, we considered a region in tile V1 (R2 in Figs. 8 and 9). This region consists of a few clumps, three of which are aligned over a filament. Among these clumps, we have chosen source # 6 of Table 3. As for the previous example, the SED (dashed line in Fig. 10) is compatible with dust at a temperature ($T = 19.7$ K) very close to the field average. The pixel-by-pixel correlation is shown by the symbols in the 250 μm panel for field V1 in Fig. 4. The excess is again associated with LVC gas, although this excess is not associated with the highest column densities available in the field. The residuals range from $R_\nu = 0.7$ (median) to 1.1 MJy sr^{-1} (peak), which could result from either a dust emissivity that is a factor 1.5 to 1.7 higher than the average for the V1 field, the presence of molecular gas with column density $N_{H_2} = 0.5$ to 0.7×10^{20} cm^{-2}, or a H I line central optical depth between 1.1 and 1.6.

The properties of the other excess regions in the field are similar. For all the sources we computed the change in dust emissivity, the H_2 column density, or the H I opacity, which could explain the residuals; these calculations are included in Table 3.

6.3. Negative residuals

So far, we discussed only the case of high positive residuals. There are, however, regions with negative residuals, in some cases so large (in absolute value) that they have been masked during the emissivity estimate. One such case is indicated by the magenta circle labeled "N" in Fig. 8 (RA = 189.02458°, Dec = 12.389513°), whose pixels are shown as diamonds in the V2 250 μm panel of Fig. 4. The negative residual corresponds to a 15′ × 30′ cloud in the LVC map, which shares the same velocity range as the neighborhood. The structure is a moderate enhancement of the neighboring gas column density with $N_H \approx 0.5 \times 10^{20}$ cm^{-2} on top of a "background" column density $N_H = 2.3 \times 10^{20}$ cm^{-2}. Most of the diffuse emission in the area comes from dust associated with this background, and this explains why the selected pixels in Fig. 4 still show the same correlation as for the diffuse field. However, the emissivity is significantly lower than the mean. These residuals could be either explained by the absence of dust in the cloud or to a much smaller emissivity than the field, resulting from a colder dust temperature in the cloud; the *missing* emission indeed corresponds to the amount of dust one would expect from the H I density enhancement for the average field emissivity. Although both interpretation are heuristically similar, a colder dust temperature seems to be excluded, since the negative residuals in this area can also be seen at the longer wavelengths.

At a lower level, negative (and positive) residuals can be found in all fields and bands, as expected from the scatter in the I_ν/N_H correlation and from the anisotropies of the CIB (see, e.g., Planck Collaboration XXX 2014). A curious case is, however, that of the V2 field, where a large area of negative residuals is coincidentally present around the center of the background Virgo cluster and inside of the cirrus ring feature. This is shown in Fig. 11, where we plot the profiles of the 100 and 250 μm residuals as a function of the projected distance from the galaxy M 87, at the center of the cluster (black lines), and we compare them with the flatter profiles obtained with the respect to the center in each of the other three HeViCS tiles (the gray lines and error bars show their average and standard deviation). The lower surface brightness inside the ring feature, when compared to the average level outside of it (in V2 and in the southern HeViCS tiles), appears as a "hole". Its presence was recognized from the

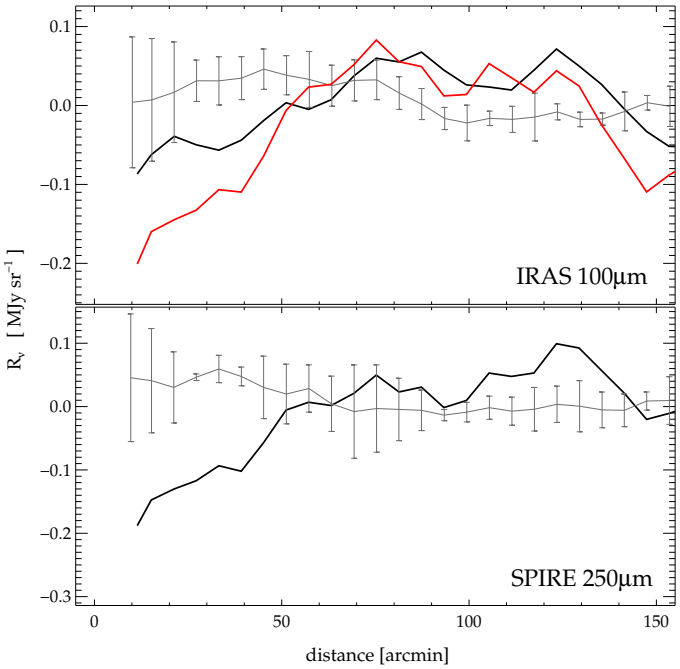

Fig. 11. Profile of the 100 and 250 μm residuals as a function of the projected distance from M 87 for the V2 field (black solid line). The gray lines and error bars are the average and standard deviation of the profiles from the center of each of the other three HeViCS tiles. The red solid line is the profile at 100 μm predicted from the 250 μm data and assuming the average 100/250 color ratio (see text for details). Each profile was obtained by azimuthally averaging the residuals over circular coronas of width 6′.

first HeViCS analysis, and was later also evident in the full sky IRAS and *Planck* surveys, from 100 μm to 550 μm.

It is not straightforward to understand whether this residual is due to a local large-scale underdensity in the CIB or to different dust properties. If the latter reason is correct then the residual could result from a lower emissivity-and thus lower cross section, since the temperature estimated within 1° from M 87, $T = 20.8$ K for $\beta = 1.59$, is very close to that for the LVC component-in a region with low gas column density ($N_{\rm H\,I} \approx 10^{20}$ cm^{-2} for the LVC). This contrasts, however, with the *excess* of emissivity seen at IRAS and *Planck* wavelength for $N_{\rm H} < 10^{20}$ cm^{-2}, which could be due to variations in the dust composition and size distribution at the lower column densities (Ysard et al. 2015), or to the contribution of dust associated with diffused ionized gas (Planck Collaboration XI 2014). On the contrary, the "hole" could only be from H II-associated dust (which we did not account for in our analysis; Sect. 3) if the column density of ionized gas is smaller inside of the feature than outside of it. However, the feature would appear as a significant dearth of Hα emission even in the available large-scale surveys, such as WHAM (Haffner et al. 2003), and this is not the case.

7. Upper limits on intracluster dust emission

Even though the topic might seem out of the scope of this paper, one of the aims of HeViCS (and of the cirrus analysis) was the detection of emission from dust in the ICM. Dust grains could be removed from cluster galaxies and transported to the ICM by the same environmental processes (such as ram pressure stripping and tidal interaction; for a review, see Boselli & Gavazzi 2006) that remove their gas content, or by internal process, such as global galactic winds. The dust passed to the ICM could in principle be detected by its reddening of background galaxies and QSOs. There is a long history of attempts at detecting such cluster reddening, but the results are still controversial and inconclusive; for instance, we compare the detection claimed by McGee & Balogh (2010) with the absence of significative excess reddening in Gutiérrez & López-Corredoira (2014).

A key issue is the ability of dust to survive destruction in the hot ICM gas (Dwek et al. 1990). For the Virgo cluster, when only environmental processes are considered, FIR emission would come predominantly from dust produced in the winds of evolved stars (Popescu et al. 2000). In this case, the predicted surface brightness is very low, 0.01 MJy sr^{-1} at 100 μm. However, in a less prohibitive scenario, in which dust is injected by galactic winds, a larger FIR contribution could come from galaxies originally on the outskirts of the cluster and falling toward the center. If the dust is able to infall within 1° from M 87, it could produce levels up to $\lesssim$0.1 MJy sr^{-1} at 175 μm (case B of Popescu et al. 2000).

The complex structure of the residuals around M 87, and in particular the large-scale negative feature discussed in Sect. 6.3, makes it complicate to detect ICM dust in Virgo. In fact, contamination from the foreground cirrus has long been recognized to be the limiting factor in detecting diffuse FIR emission from clusters (Wise et al. 1993; Stickel et al. 2002; Bai et al. 2007; Kitayama et al. 2009).

Following Stickel et al. (1998), we have attempted to measure an excess in Virgo at 100 μm with respect to 250 μm. We used the 250 μm V2 map to estimate the 100 μm emission that would be expected on the basis of the average 100/250 color ratio (1.025, measured on field V2). This estimate is shown with the red line in Fig. 11. Indeed, the profile of the *true* residuals reveals a 100 μm emission in excess of the predicted emission. The excess is $\approx$0.1 MJy sr^{-1} in the cluster center, a value close to the detection claimed by Stickel et al. (1998) in Coma, to the models of Dwek et al. (1990) for the Coma cluster, and to the more optimistic predictions of intracluster dust emission in Virgo by Popescu et al. (2000). It is also close, however, to the upper limits of 0.06 MJy sr^{-1} estimated using *Spitzer* data at 70 and 160 μm by Kitayama et al. (2009), who dismissed the dust detection in the Coma cluster by Stickel et al. (1998) as due to cirrus contamination. We are not able therefore to confirm that the excess is due to cluster emission, since it is of the same order as the noise in the residuals and in the random profiles centered on the other fields (gray lines and error bars in Fig. 11), which are caused by both variations in the dust emissivity and by the variance of the CIB (Planck Collaboration XI 2014). The issue is further complicated by the decorrelation between the 100 μm CIB power spectrum and that at longer wavelengths (Planck Collaboration XXX 2014).

Notably, most of the truly intergalactic features (optically highlighted by Mihos et al. 2005) cannot be seen in dust emission. The only exception is the plume to the north of NGC 4435/NGC 4438, which Cortese et al. (2010) found to be most likely a foreground cirrus cloud rather than a tidal tail in the cluster. In fact, the only features of the deep optical survey of Virgo presented by Mihos (2015) clearly associated with emission in our maps are those corresponding to the highest column densities of the Galactic H I.

8. Summary and conclusions

We have studied the correlation between FIR emission and atomic gas column density for the low density, high Galactic

latitude cirrus in the foreground of the Virgo cluster. For the dust emission, we used the HeViCS maps at 250, 350, and 500 μm obtained with the SPIRE instrument aboard the *Herschel* Space Observatory (Davies et al. 2010a, 2012; Auld et al. 2013); maps at 60 and 100 μm obtained from the IRAS-IRIS data set (Miville-Deschênes & Lagache 2005) and HFI maps at 350, 550 and 850 μm from the 2013 *Planck* data release (Planck Collaboration I 2014). Two H I column density maps were obtained from the ALFALFA survey (Giovanelli et al. 2005), separating an IVC component with emission at velocities in the range $-100 < v_{\rm LSR}/{\rm km\,s^{-1}} < -20$ and a LVC component with $-20 < v_{\rm LSR}/{\rm km\,s^{-1}} < 100$. For each band and for each of the four HeViCS fields, we derived the dust emissivity associated with the two gas components.

We find that the values of the emissivities for dust associated with the LVC are consistent with the determinations by Planck Collaboration XI (2014) and Planck Collaboration Int. XVII (2014). In the SPIRE bands we measure $\epsilon_\nu^{\rm LVC} = (0.787 \pm 0.077)$, (0.395 ± 0.034) and $(0.171 \pm 0.032) \times 10^{-20}$ MJy sr^{-1} cm^2 at 250, 350, and 500 μm, respectively. The values represent the average and the standard deviation of the emissivities derived for each of the $\approx 4^\circ \times 4^\circ$ HeViCS fields. The scatter in the emissivity values is generally larger than the uncertainties estimated for each individual field and points toward intrinsic field-to-field variations. Indeed, the scatter measured in the analysis of *Planck* data (covering a much larger range of column density than HeViCS) suggests variation of the dust properties along different lines of sight and environments (Ysard et al. 2015; Fanciullo et al. 2015). Yet it is remarkable that the average values derived for the HeViCS footprint, covering just 0.2% of the sky, are in excellent agreement (see Fig. 7) with the analysis of high-latitude dust emission by the Planck team, covering from 20% (Planck Collaboration Int. XVII 2014) to 50% (Planck Collaboration XI 2014) of the sky.

By fitting the average emissivity SED with a MBB, we derived a dust absorption cross section,

$$\frac{\tau_\nu^{\rm LVC}}{N_{\rm H\,I}} = (0.49 \pm 0.13) \times \left(\frac{250\,\mu{\rm m}}{\lambda}\right)^{1.53\pm0.17} \times 10^{-25}\ {\rm cm^2\,H^{-1}},$$

with an average dust temperature $T = 20.4 \pm 1.5$ K. Again, this is consistent with the values derived by Planck Collaboration XI (2014) and Planck Collaboration Int. XVII (2014). In particular the planet-calibrated SPIRE data confirms the lower emissivity, absorption cross-section (and spectral index) with respect to the FIRAS spectrum and calls for a revisitation of the FIRAS-calibrated dust models (e.g., Draine 2003; Zubko et al. 2004; Compiègne et al. 2011; Jones et al. 2013). Nevertheless, we found that the dust absorption cross section used in most of the HeViCS papers results in only a slight underestimate of the dust mass in a galaxy with respect to those obtained with the value above (see Appendix B).

Dust associated with the IVC component has lower emissivity than the LVC component, $\epsilon_\nu^{\rm IVC} = (0.408 \pm 0.054)$, (0.186 ± 0.026) and $(0.0588 \pm 0.00023) \times 10^{-20}$ MJy sr^{-1} cm^2 at 250, 350, and 500 μm; the IVC component also has a bluer spectrum, resulting in a hotter dust temperature when fitted with a MBB, and in a lower dust cross section. These results confirm the early analysis of *Planck* data for high-latitude clouds, and point toward different properties of dust in the IVC with respect to the LVC (Planck Collaboration XXIV 2011).

The high resolution of the ALFALFA data allowed us to study the departure of the H I-dust correlation at scales smaller that ~20′. This corresponds to (uncertain) linear sizes of 0.6–0.9 pc, assuming as a distance the scale height of the global MW emission from cold dust (100 pc; Misiriotis et al. 2006) or the scale height of the H I disk (150 pc; Kalberla & Kerp 2009), respectively. We found regions with residuals significantly higher than the average scatter of the correlation. The high residual regions are most probably the result of local variation in the dust properties (increase in the dust emissivity by 20 to 80%) or excess emission associated with molecular clouds of average column density $N_{\rm H_2} \lesssim 10^{20}$ cm^{-2}. We also found regions of negative residuals and, in particular, a H I feature of the LVC component with no associated dust emission. This parcel of gas devoid of dust seems to suggest that besides changes in the grain composition and size distribution, the scatter in the emissivity measurements could be due to an imperfect spatial correspondence between the ISM tracers at these smaller scales; on the other hand, dedicated observations of molecular gas tracers are needed to see if the excess emission can be due to (so far) untraced gas or dust clouds devoid of a gas component.

Because of the cirrus contamination and large residuals in the proximity of the center of the Virgo cluster, we find no strong evidence for dust emission from the ICM. In fact, even for the most optimistic prediction for the Virgo cluster (Popescu et al. 2000) the surface brightness is not likely to exceed ≈ 0.1 MJy sr^{-1} at 100 μm; this surface brightness level is the same as the average scatter of the residuals and, in most cases, is dominated by CIB fluctuations.

This work was dedicated to the study of the cirrus absorption properties in the FIR/submm. The availability of deep UV (Boissier et al. 2015), optical (Ferrarese et al. 2012; Mihos 2015) and atomic gas (Giovanelli et al. 2005; Peek et al. 2011) surveys of the Virgo cluster will also allow a study of the emissivity of scattered starlight in the future, thus posing further constraints on the dust grain models for the high Galactic latitude cirrus.

Acknowledgements. We are grateful to Edvige Corbelli, Luca Cortese, Emmanuel Xilouris, and an anonymous referee for comments that improved the quality of the paper. S.B., J.I.D., M. Baes, M. Bocchio, V.C., C.J.R.C., A.J., S.M. acknowledge support from the European Research Council (ERC) in the form of the FP7 project DustPedia (P. I. Jonathan Davies, proposal 606824). S.B., C.G., L.K.H. are grateful for support from PRIN-INAF 2012/13. The ALFALFA team at Cornell was supported by the NSF grants AST-0607007 and AST-1107390 to R.G. and M.H. and by grants of the Brinson Foundation to M.H. S.Z. has been supported by the EU Marie Curie Career Integration Grant "SteMaGE" Nr. PCIG12-GA-2012-326466 (Call Identifier: FP7-PEOPLE-2012 CIG). Based on observations obtained with *Planck* (`http://www.esa.int/Planck`), an ESA science mission with instruments and contributions directly funded by ESA Member States, NASA, and Canada. This research has made use of: APLpy, an open-source plotting package for Python hosted at `http://aplpy.github.com`; the NASA/IPAC Extragalactic Database (NED), which is operated by the Jet Propulsion Laboratory, California Institute of Technology, under contract with the National Aeronautics and Space Administration; NASA's Astrophysics Data System.

References

Auld, R., Bianchi, S., Smith, M. W. L., et al. 2013, MNRAS, 428, 1880
Bai, L., Rieke, G. H., & Rieke, M. J. 2007, ApJ, 668, L5
Bertin, E., & Arnouts, S. 1996, A&AS, 117, 393
Bertin, E., Mellier, Y., Radovich, M., et al. 2002, in Astronomical Data Analysis Software and Systems XI, eds. D. A. Bohlender, D. Durand, & T. H. Handley, ASP Conf. Ser., 281, 228
Bertincourt, B., Lagache, G., Martin, P. G., et al. 2016, A&A, 588, A107
Béthermin, M., Le Floc'h, E., Ilbert, O., et al. 2012, A&A, 542, A58
Bianchi, S. 2013, A&A, 552, A89
Bianchi, S., Davies, J. I., & Alton, P. B. 2000, A&A, 359, 65
Bocchio, M., Jones, A. P., Verstraete, L., et al. 2013, A&A, 556, A6
Bocchio, M., Jones, A. P., & Slavin, J. D. 2014, A&A, 570, A32
Boissier, S., Boselli, A., Voyer, E., et al. 2015, A&A, 579, A29

Bolatto, A. D., Wolfire, M., & Leroy, A. K. 2013, ARA&A, 51, 207
Boselli, A., & Gavazzi, G. 2006, PASP, 118, 517
Boselli, A., Ciesla, L., Buat, V., et al. 2010a, A&A, 518, L61
Boselli, A., Eales, S., Cortese, L., et al. 2010b, PASP, 122, 261
Boselli, A., Ciesla, L., Cortese, L., et al. 2012, A&A, 540, A54
Boulanger, F., & Perault, M. 1988, ApJ, 330, 964
Boulanger, F., Abergel, A., Bernard, J.-P., et al. 1996, A&A, 312, 256
Bracco, A., Cooray, A., Veneziani, M., et al. 2011, MNRAS, 412, 1151
Clark, C. J. R., Schofield, S. P., Gomez, H. L., & Davies, J. I. 2016, MNRAS, 459, 1646
Compiègne, M., Verstraete, L., Jones, A., et al. 2011, A&A, 525, A103
Condon, J. J., Cotton, W. D., Greisen, E. W., et al. 1998, AJ, 115, 1693
Cortese, L., Bendo, G. J., Isaak, K. G., Davies, J. I., & Kent, B. R. 2010, MNRAS, 403, L26
Dale, D. A., Aniano, G., Engelbracht, C. W., et al. 2012, ApJ, 745, 95
Davies, J. I., Baes, M., Bendo, G. J., et al. 2010a, A&A, 518, L48
Davies, J. I., Wilson, C. D., Auld, R., et al. 2010b, MNRAS, 409, 102
Davies, J. I., Bianchi, S., Cortese, L., et al. 2012, MNRAS, 419, 3505
Desert, F. X., Bazell, D., & Boulanger, F. 1988, ApJ, 334, 815
Désert, F. X., Boulanger, F., & Puget, J. L. 1990, A&A, 237, 215
Draine, B. T. 2003, ARA&A, 41, 241
Draine, B. T. 2011, Physics of the Interstellar and Intergalactic Medium (Princeton University Press)
Draine, B. T., & Lee, H. M. 1984, ApJ, 285, 89
Draine, B. T., Dale, D. A., Bendo, G., et al. 2007, ApJ, 663, 866
Dwek, E., Rephaeli, Y., & Mather, J. C. 1990, ApJ, 350, 104
Fanciullo, L., Guillet, V., Aniano, G., et al. 2015, A&A, 580, A136
Ferrarese, L., Côté, P., Cuillandre, J.-C., et al. 2012, ApJS, 200, 4
Finkbeiner, D. P. 2003, ApJS, 146, 407
Gillmon, K., & Shull, J. M. 2006, ApJ, 636, 908
Giovanelli, R., Haynes, M. P., Kent, B. R., et al. 2005, AJ, 130, 2598
Giovanelli, R., Haynes, M. P., Kent, B. R., et al. 2007, AJ, 133, 2569
Gispert, R., Lagache, G., & Puget, J. L. 2000, A&A, 360, 1
Griffin, M. J., Abergel, A., Abreu, A., et al. 2010, A&A, 518, L3
Gutiérrez, C. M., & López-Corredoira, M. 2014, A&A, 571, A66
Haffner, L. M., Reynolds, R. J., Tufte, S. L., et al. 2003, ApJS, 149, 405
Hartmann, D., Magnani, L., & Thaddeus, P. 1998, ApJ, 492, 205
Heiles, C., & Troland, T. H. 2003, ApJS, 145, 329
Heithausen, A. 2002, A&A, 393, L41
Heithausen, A. 2007, in SINS – Small Ionized and Neutral Structures in the Diffuse Interstellar Medium, eds. M. Haverkorn, & W. M. Goss, ASP Conf. Ser., 365, 177
Heithausen, A. 2012, A&A, 543, A21
Helou, G., & Walker, D. W. 1988, Infrared astronomical satellite (IRAS) catalogs and atlases, Vol. 7, The small scale structure catalog, NASA-RP-1190, Tech. Rep.
Hunt, L. K., Draine, B. T., Bianchi, S., et al. 2015, A&A, 576, A33
James, A., Dunne, L., Eales, S., & Edmunds, M. G. 2002, MNRAS, 335, 753
Jones, A. P., Fanciullo, L., Köhler, M., et al. 2013, A&A, 558, A62
Juvela, M., Ristorcelli, I., Marshall, D. J., et al. 2015, A&A, 584, A93
Kalberla, P. M. W., & Kerp, J. 2009, ARA&A, 47, 27
Kalberla, P. M. W., Burton, W. B., Hartmann, D., et al. 2005, A&A, 440, 775
Kelly, B. C., Shetty, R., Stutz, A. M., et al. 2012, ApJ, 752, 55
Kitayama, T., Ito, Y., Okada, Y., et al. 2009, ApJ, 695, 1191
Köhler, M., Ysard, N., & Jones, A. P. 2015, A&A, 579, A15
Kuntz, K. D., & Danly, L. 1996, ApJ, 457, 703
Lagache, G., Abergel, A., Boulanger, F., Désert, F. X., & Puget, J. L. 1999, A&A, 344, 322
Lagache, G., Haffner, L. M., Reynolds, R. J., & Tufte, S. L. 2000, A&A, 354, 247
Low, F. J., Young, E., Beintema, D. A., et al. 1984, ApJ, 278, L19
Magrini, L., Bianchi, S., Corbelli, E., et al. 2011, A&A, 535, A13
Markwardt, C. B. 2009, in Astronomical Data Analysis Software and Systems XVIII, ed. D. A. Bohlender, D. Durand, & P. Dowler, ASP Conf. Ser., 411, 251
Mathis, J. S., Mezger, P. G., & Panagia, N. 1983, A&A, 128, 212
McGee, S. L., & Balogh, M. L. 2010, MNRAS, 405, 2069
Mihos, C. 2015, in The General Assembly of Galaxy Halos, IAU Symp., 22
Mihos, J. C., Harding, P., Feldmeier, J., & Morrison, H. 2005, ApJ, 631, L41
Misiriotis, A., Xilouris, E. M., Papamastorakis, J., Boumis, P., & Goudis, C. D. 2006, A&A, 459, 113
Miville-Deschênes, M., & Lagache, G. 2005, ApJS, 157, 302
Neugebauer, G., Habing, H. J., van Duinen, R., et al. 1984, ApJ, 278, L1
Ossenkopf, V., & Henning, T. 1994, A&A, 291, 943
Ott, S. 2010, in ASP Conf. Ser., 434, 139
Pappalardo, C., Bendo, G. J., Bianchi, S., et al. 2015, A&A, 573, A129
Peek, J. E. G., Heiles, C., Douglas, K. A., et al. 2011, ApJS, 194, 20
Pilbratt, G. L., Riedinger, J. R., Passvogel, T., et al. 2010, A&A, 518, L1
Planck Collaboration XXIII. 2011, A&A, 536, A23
Planck Collaboration XXIV. 2011, A&A, 536, A24
Planck Collaboration I. 2014, A&A, 571, A1
Planck Collaboration VIII. 2014, A&A, 571, A8
Planck Collaboration IX. 2014, A&A, 571, A9
Planck Collaboration XI. 2014, A&A, 571, A11
Planck Collaboration XII. 2014, A&A, 571, A12
Planck Collaboration XIII. 2014, A&A, 571, A13
Planck Collaboration XIV. 2014, A&A, 571, A14
Planck Collaboration XXX. 2014, A&A, 571, A30
Planck Collaboration XXVIII. 2016, A&A, 594, A28
Planck Collaboration Int. XVII. 2014, A&A, 566, A55
Planck Collaboration Int. XXV. 2015, A&A, 582, A28
Planck Collaboration Int. XXIX. 2016, A&A, 586, A132
Poglitsch, A., Waelkens, C., Geis, N., et al. 2010, A&A, 518, L2
Popescu, C. C., & Tuffs, R. J. 2013, MNRAS, 436, 1302
Popescu, C. C., Tuffs, R. J., Fischera, J., & Völk, H. 2000, A&A, 354, 480
Reach, W. T., Wall, W. F., & Odegard, N. 1998, ApJ, 507, 507
Reach, W. T., Heiles, C., & Bernard, J.-P. 2015, ApJ, 811, 118
Rudick, C. S., Mihos, J. C., Harding, P., et al. 2010, ApJ, 720, 569
Schlegel, D. J., Finkbeiner, D. P., & Davis, M. 1998, ApJ, 500, 525
Shetty, R., Kauffmann, J., Schnee, S., & Goodman, A. A. 2009, ApJ, 696, 676
Smith, M. W. L. 2012, Ph.D. Thesis, Cardiff University
Smith, M. W. L., Vlahakis, C., Baes, M., et al. 2010, A&A, 518, L51
Spitzer, L. 1978, Physical Processes in the Interstellar Medium (New York: Wiley)
Stickel, M., Lemke, D., Mattila, K., Haikala, L. K., & Haas, M. 1998, A&A, 329, 55
Stickel, M., Klaas, U., Lemke, D., & Mattila, K. 2002, A&A, 383, 367
Veneziani, M., Ade, P. A. R., Bock, J. J., et al. 2010, ApJ, 713, 959
Wakker, B. P. 2001, ApJS, 136, 463
Wakker, B. P., & van Woerden, H. 1997, ARA&A, 35, 217
Wise, M. W., O'Connell, R. W., Bregman, J. N., & Roberts, M. S. 1993, ApJ, 405, 94
Witt, A. N., Gold, B., Barnes, III, F. S., et al. 2010, ApJ, 724, 1551
Ysard, N., Köhler, M., Jones, A., et al. 2015, A&A, 577, A110
Zubko, V., Dwek, E., & Arendt, R. G. 2004, ApJS, 152, 211

Appendix A: Offsets and zodiacal light gradients

We discuss here the offsets O_ν and the ecliptic latitude gradient E_ν resulting from the fitting described in Sects. 3 and 4.

The derived O_ν are shown in the left panel of Fig. A.1. For the IRIS 60 μm, the offset is positive, small, and very similar for all fields. At 100 μm, it is larger and likely dominated by uncertainties in the subtraction of the zodiacal light contribution from IRIS maps: this is discussed in Planck Collaboration XI (2014), where a correction is found by comparing smoothed IRIS images with the earlier 100 μm maps from Schlegel et al. (1998), which implemented a different, empirical, zodiacal light subtraction. When this correction is taken into account, our values of O_ν are compatible with those derived by Planck Collaboration XI (2014) by correlating dust emission and atomic gas data on their *Low* $N_{\rm HI}$ mask. The offsets we found for *Planck* data are also compatible with the values derived on the same sky area by Planck Collaboration VIII (2014). The offsets derived for SPIRE data are instead negative, since the maps by construction have their median level set to zero: fields with larger emission (V1 and V2 at 250 μm) have a median level biased to more positive values, and the offset is more negative. As a crosscheck, we also derived the offset between SPIRE and *Planck*-HFI maps using the `zeroPointCorrection` task within HIPE. The *Planck* maps used by the task have been corrected so that they also include the emission from the CIB. Thus our offset can be compared with the difference between the CIB estimate used by the *Planck* team (Planck Collaboration VIII 2014) and the HIPE offset. These values (shown as crosses at 250, 350 and 500 μm in the left panel of Fig. A.1) are compatible with those derived here at 250 μm (the HIPE offset resulting from a spectrum extrapolation) but show some differences at the longer wavelengths. A possible explanation might be in the uncertainties in the zero-level determination or in the spectral baseline subtraction of H I maps, that might result in different correlations between dust emission and gas and between two dust emission channels, as noted also by Planck Collaboration VIII (2014). For the same reason, intensity levels estimated using Eq. (1) in two adjacent HeViCS fields might not overlap. However, in all cases these residual offsets are $\lesssim 1\sigma$.

The right panel of Fig. A.1 shows the fitted ecliptic latitude gradient, E_ν. In half of the fits (see Table 1), the derived E_ν is found to be insignificant ($<3\sigma$). When measured at $>3\sigma$, it is generally consistent between SPIRE and HFI bands (i.e. always positive for fields V1 and V4, always negative for V3). However, we found it to be present also in HFI maps, which were already corrected for zodiacal light; and the V1 field has a larger gradient than V2 (where it is almost always consistent with zero), despite their common extent in ecliptic latitude. Either our naïve choice for the gradient is not able to capture the complexity of a full zodiacal light model (see Planck Collaboration XIV 2014, for the modeling of Zodiacal light in HFI maps) or it could possibly hide, as we discussed for O_ν, spatial gradients due to uncertainties in the H I spectra baseline subtraction. Gradients are also found for the IRIS data: at 100 μm, gradients are found to be of the same order of what can be derived from the zodiacal light subtraction of Planck Collaboration XI (2014) (crosses in the right panel of Fig. A.1). However, the largest (negative) gradient derived here is for field V1, while using the Planck Collaboration XI (2014) correction it is for field V4. Whatever is the true nature of E_ν, we nevertheless retained the term in the fit because we found that it greatly reduced the scatter in the determination of the dust emissivities associated with the IVC component, without modifying significantly the results for the LVC component.

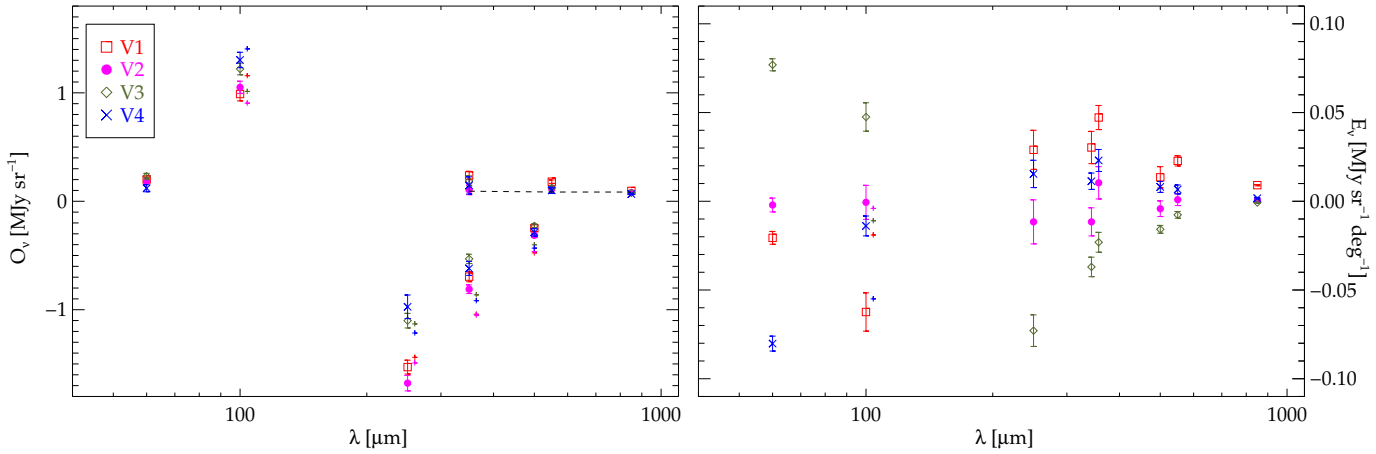

Fig. A.1. *Left panel*: offsets O_ν. We also indicate with crosses estimates at 100 μm obtained summing the offset with LAB data and the residual zodiacal light contamination in IRIS maps as derived by Planck Collaboration XI (2014); estimates for SPIRE data using the SPIRE/HFI offsets from the `zeroPointCorrection` procedure in HIPE. The dashed line shows the offset derived by the *Planck* team on zodi-corrected maps (Planck Collaboration VIII 2014). *Right panel*: fitted gradient in ecliptic latitude E_ν. Crosses show the gradient as derived from the correction described in Planck Collaboration XI (2014). To avoid cluttering, we have slightly displaced some symbols from their exact wavelength.

Appendix B: Implications for the estimate of dust mass in external galaxies

The absorption cross section of high-latitude MW dust is typically used as a proxy for the properties of dust in external galaxies. We evaluate here the impact of the new MW LVC cross section found in *Planck* papers and in the current one, when these are used to derive the dust masses.

Bianchi (2013) argued that, under the common assumption that the FIR SED is due to dust heated by an average ISRF (Draine et al. 2007; Dale et al. 2012), fits using a single temperature MBB – essentially, using a single dust grain of average absorption cross section – do not perform much worse than fits using more realistic dust models, with distributions of grain sizes of different materials. Assuming the same dust-to-gas mass ratio (∼0.01) as derived for the Compiègne et al. (2011) dust model, and adopting their correction to account for hydrogen atoms in the ionized and molecular gas (increasing the hydrogen column density by 23%), we can derive from the current data an average dust absorption cross section per unit of mass $\kappa_{\rm abs}(250\ \mu{\rm m}) = 2.2 \pm 0.6\,{\rm cm^2\,g^{-1}}$ (with $\beta = 1.5$). On the same sample of galaxies used in Bianchi (2013), the dust mass derived using this cross section would be on average a factor 1.55 larger than that obtained using the average properties of the FIRAS-constrained Compiègne et al. (2011) dust model with $\kappa_{\rm abs}(250\ \mu{\rm m}) = 5.1\,{\rm cm^2\,g^{-1}}$ ($\beta = 1.91$). In several papers of the HeViCS series we instead used $\kappa_{\rm abs}(350\ \mu{\rm m}) = 1.92\,{\rm cm^2\,g^{-1}}$ ($\beta = 2$). Accidentally[2], the dust masses obtained with this value are very close to those obtained with the new absorption cross section, which is on average lower by 5%. Because of the lower spectral index of the new cross section, the fitted temperature would be larger, the average for the sample being ∼25 K, instead of ∼21 and 22 K obtained with the Compiègne et al. (2011) model spectral index and the $\beta = 2$ HeViCS choice, respectively.

Clark et al. (2016) estimated the dust absorption cross section from integrated FIR/submm SEDs and properties for 22 galaxies in the Herschel Reference Survey (HRS; Boselli et al. 2010b). They used the mass of metals as a proxy of the dust mass and assumed a power law for the cross-section spectrum, following the method by James et al. (2002). If their analysis is repeated using $\beta = 1.5$, as suggested by this work, it is found that $\kappa_{\rm abs}(250\ \mu{\rm m}) = 1.02^{+1.09}_{-0.49}\,{\rm cm^2\,g^{-1}}$. The average value is lower than the estimates based on DHGL emission by a factor two, and thus the dust masses would be higher by the same factor. The discrepancy might suggest that dust in the DHGL medium has different average properties than the bulk of the dust mass in a galaxy. If this is true, dust masses might be better estimated from global SEDs using the cross sections from Clark et al. (2016); yet, the DHGL value is still within the large scatter of their estimates, which might point to galaxy-to-galaxy variations of the average dust properties.

Finally, a value $\beta \approx 1.5$ is compatible with the SPIRE colors of the HRS galaxies (Boselli et al. 2010a, 2012). The trend in SPIRE colors could however be produced by subtle effects, such as deviations from a pure power law in a restricted wavelength range or by the mixing of the dust temperatures for grains of different material and size (Hunt et al. 2015). This reminds us that the result of the present work might just be an apparent β value providing a good description of the emissivity SED, but hiding the complexity of the dust grain mixture producing it.

Appendix C: Data, models, and residuals

Figures C.1 to C.7 show the observed dust emission, the dust emission modeled from the H I observations, and the residuals in the IRAS 60 and 100 μm bands, the SPIRE and HFI 350 μm bands, the SPIRE 500 μm band and the HFI 550 μm band, and the HFI 850 μm band, respectively. Images follow the same criteria used to present the results for the SPIRE 250 μm band in Fig. 8.

[2] The average cross section used in most HeViCS papers (see, e.g., Smith et al. 2010; Magrini et al. 2011; Davies et al. 2012; Auld et al. 2013) was taken from the MW dust model of Draine (2003). Even though the model was constrained on the FIRAS spectrum, its emission under the LISRF heating was lower than the (corrected) DHGL SED of Compiègne et al. (2011). Bianchi (2013) maintained that this could be due to a different correction for the contribution of ionized (and molecular) gas to the hydrogen column density. Inconsistencies between *Planck* observations and the Draine (2003) models were also noted by Planck Collaboration Int. XVII (2014) and Planck Collaboration Int. XXIX (2016).

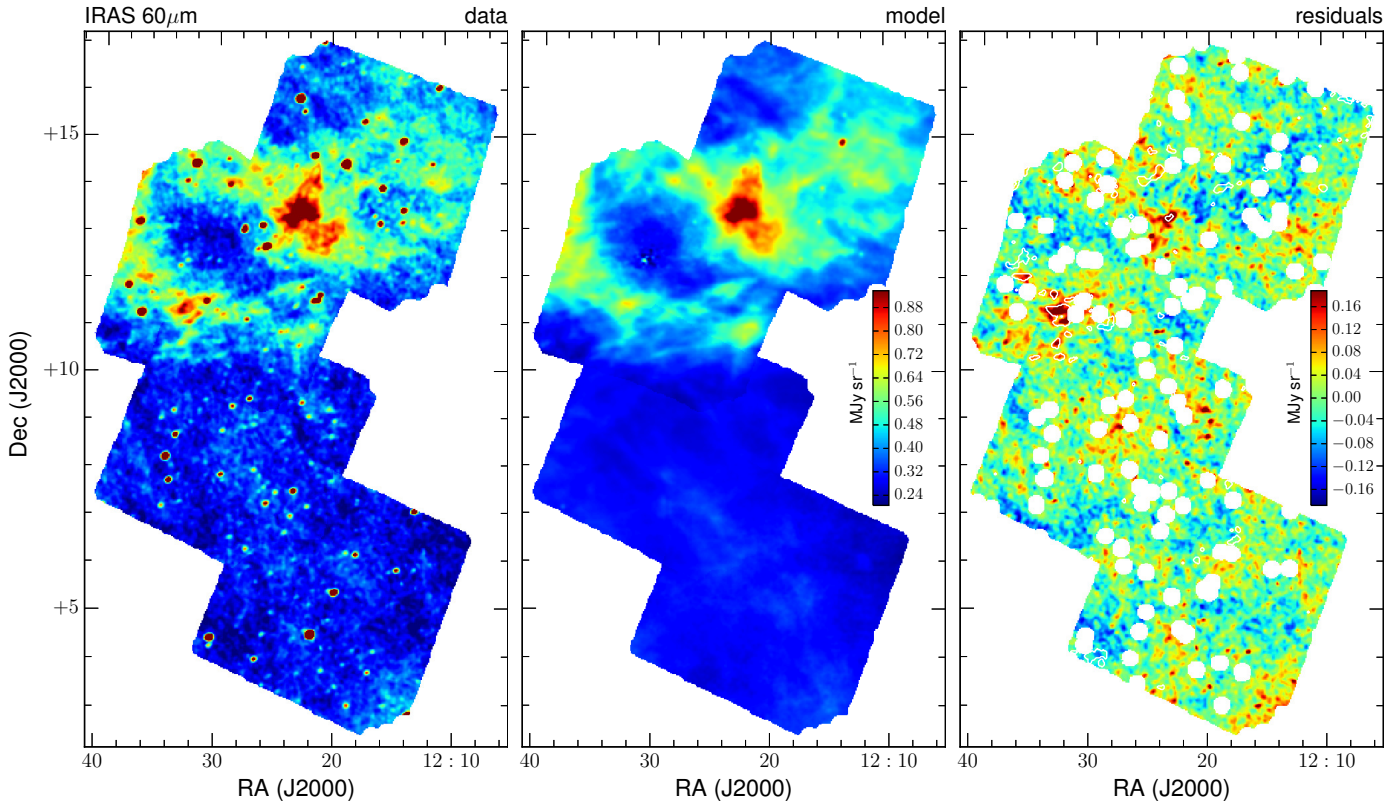

Fig. C.1. Same as Fig. 8, but for the IRAS 60 μm band.

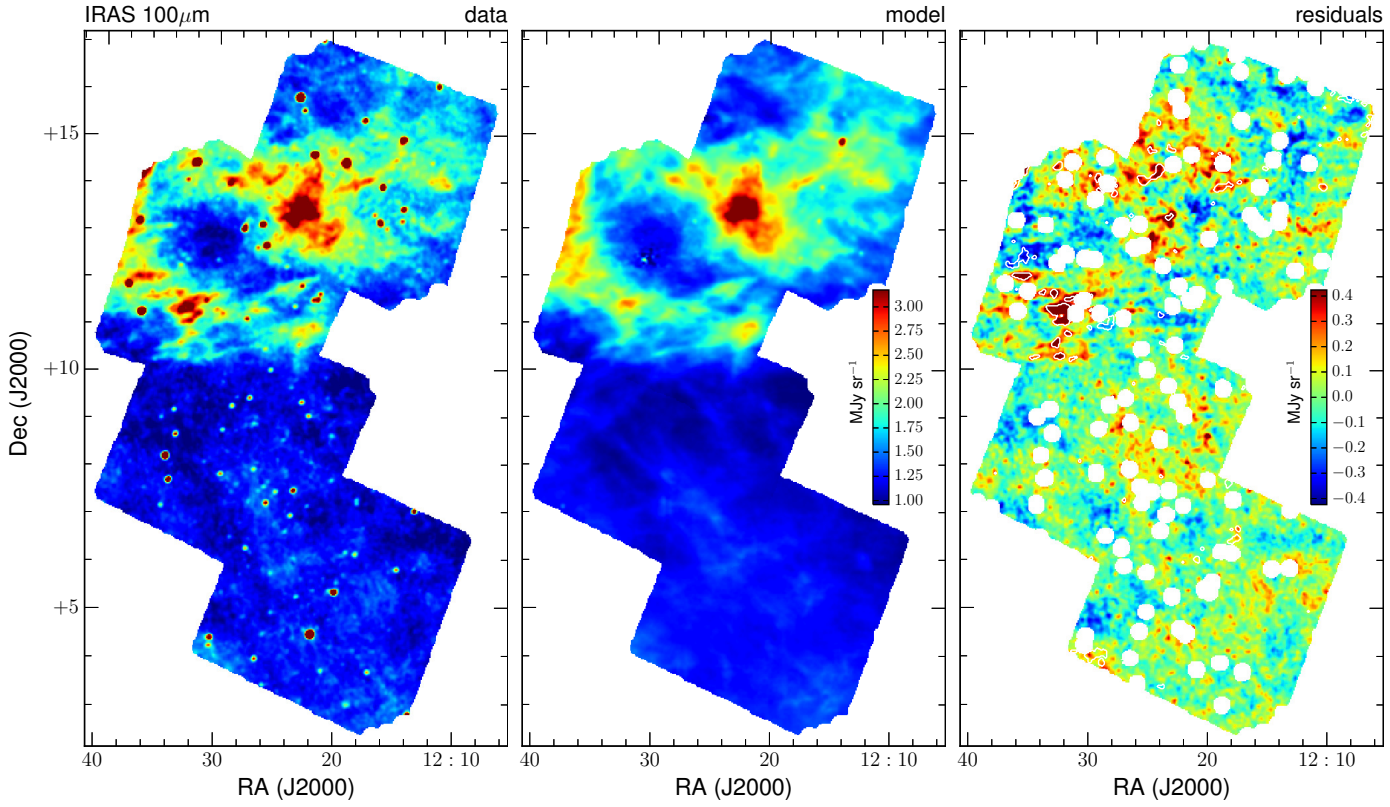

Fig. C.2. Same as Fig. 8, but for the IRAS 100 μm band.

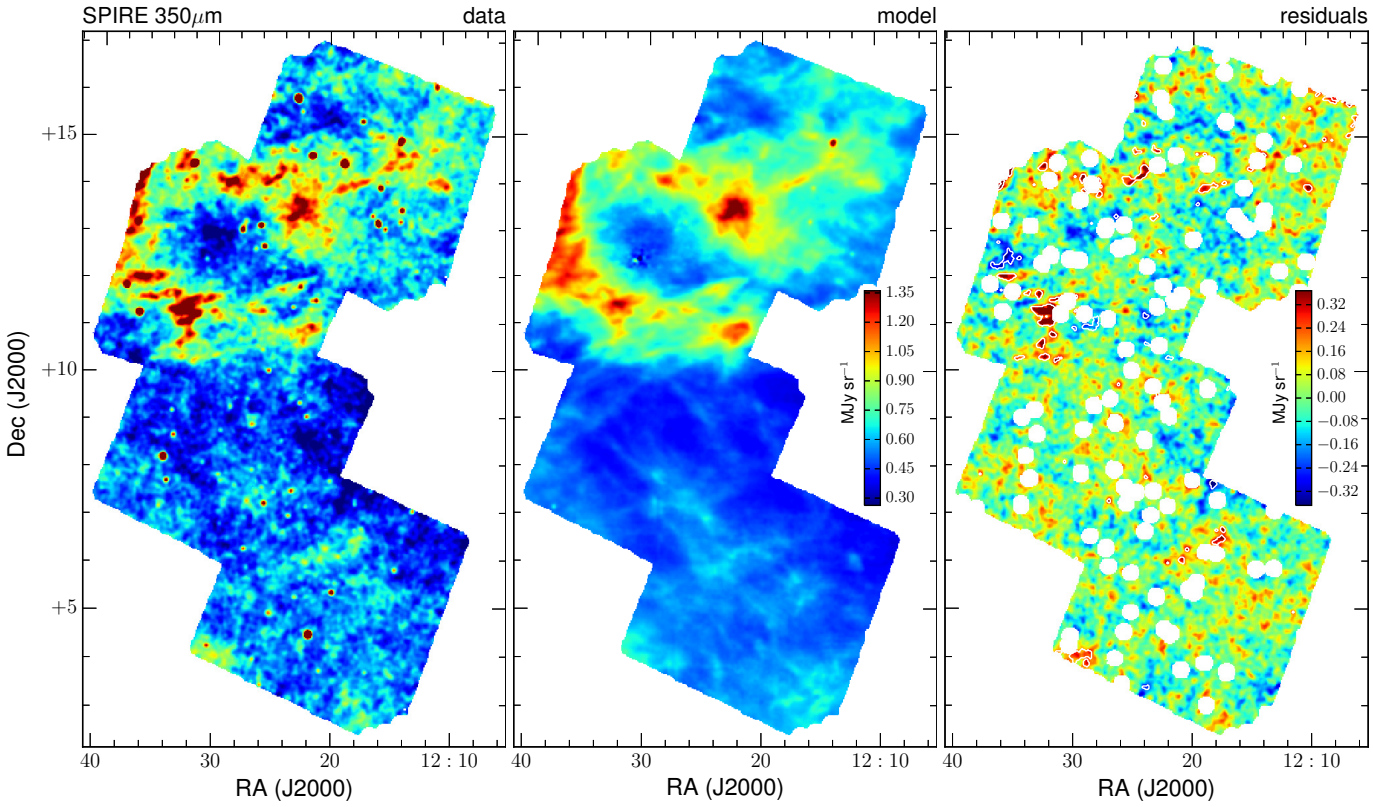

Fig. C.3. Same as Fig. 8, but for the SPIRE 350 μm band.

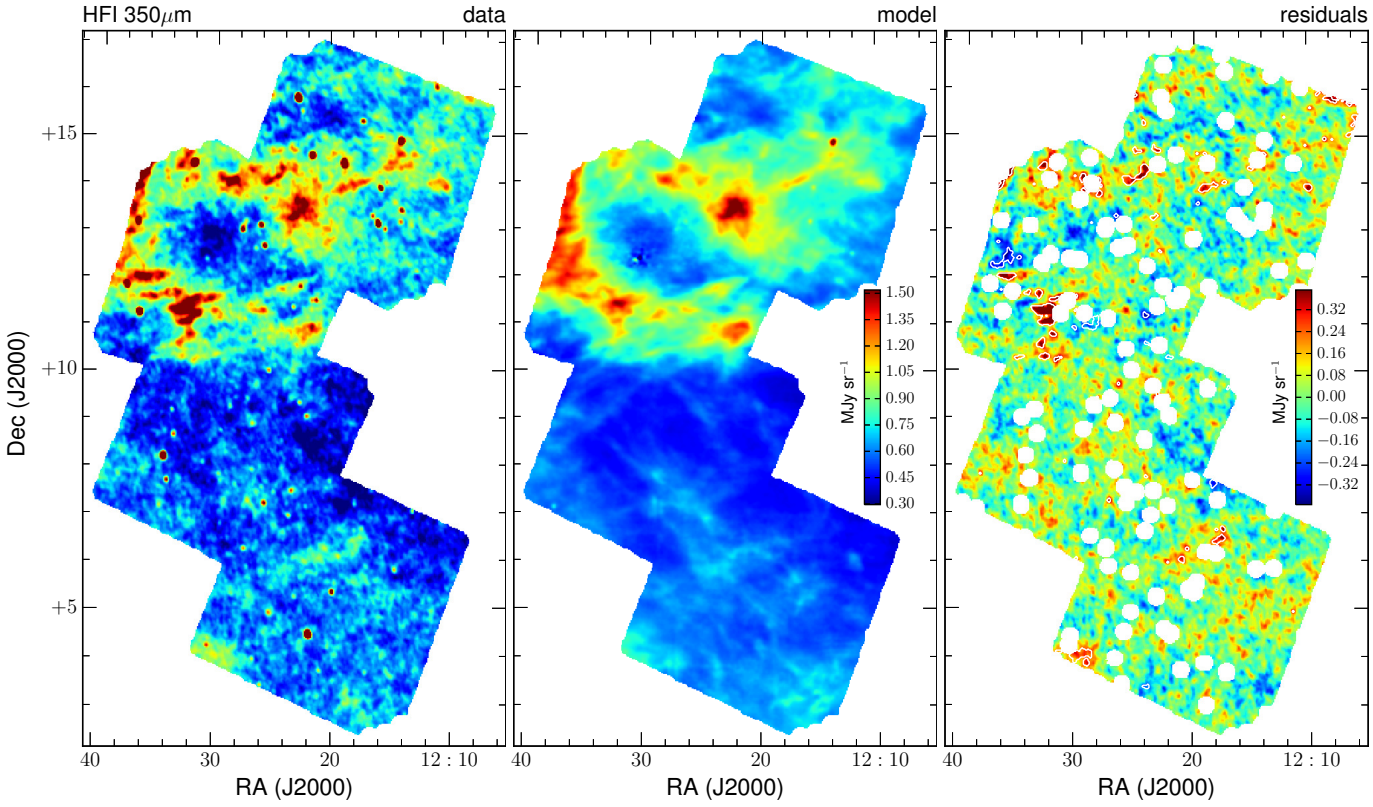

Fig. C.4. Same as Fig. 8, but for the HFI 350 μm band.

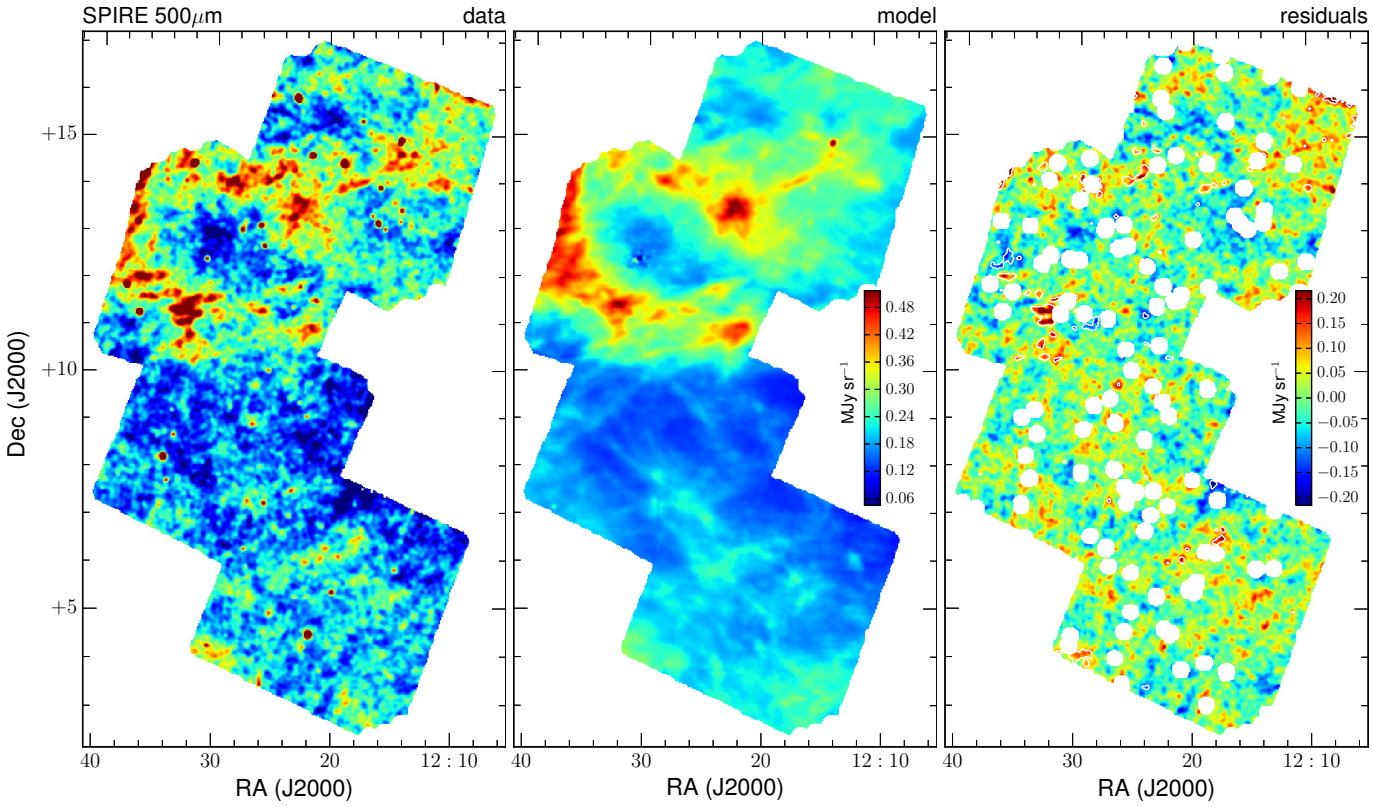

Fig. C.5. Same as Fig. 8, but for the SPIRE 500 μm band.

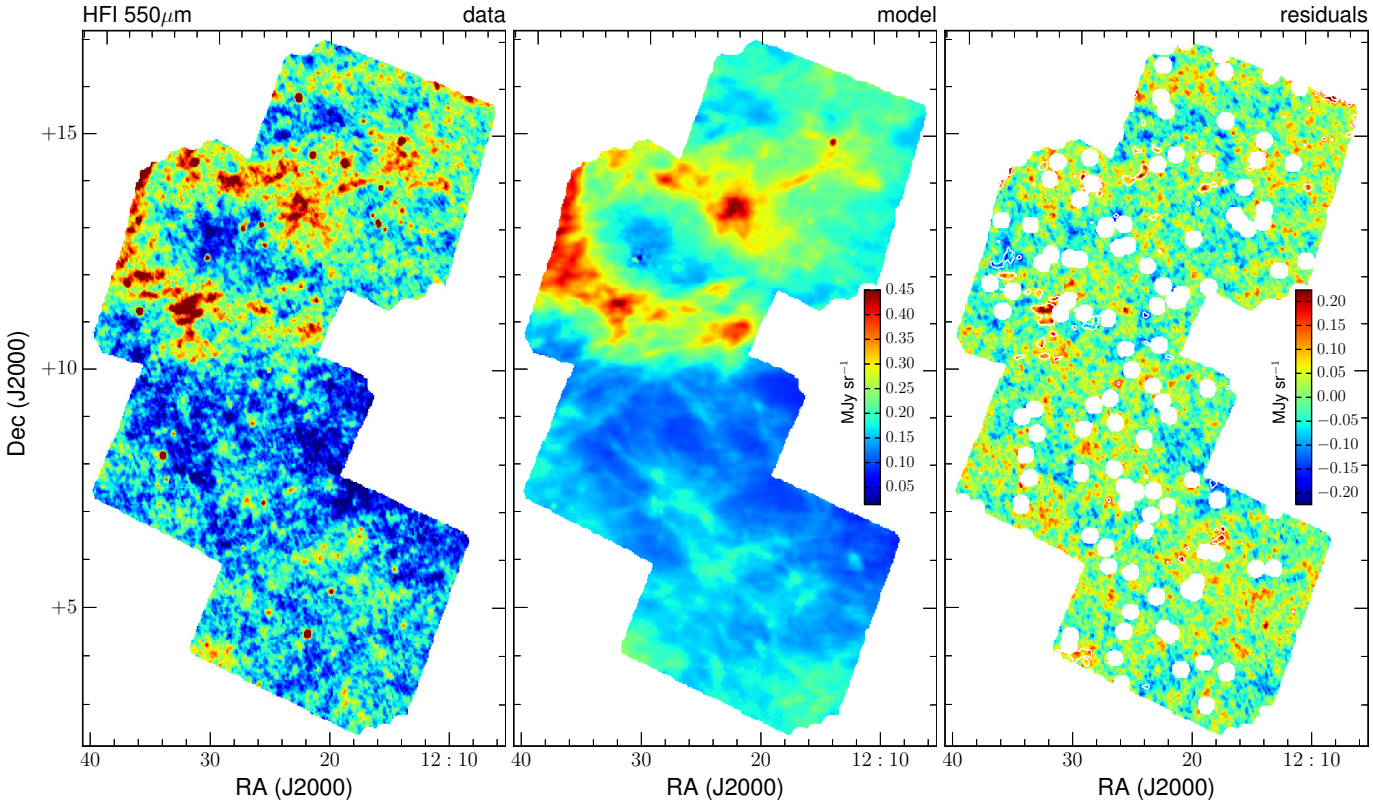

Fig. C.6. Same as Fig. 8, but for the HFI 550 μm band.

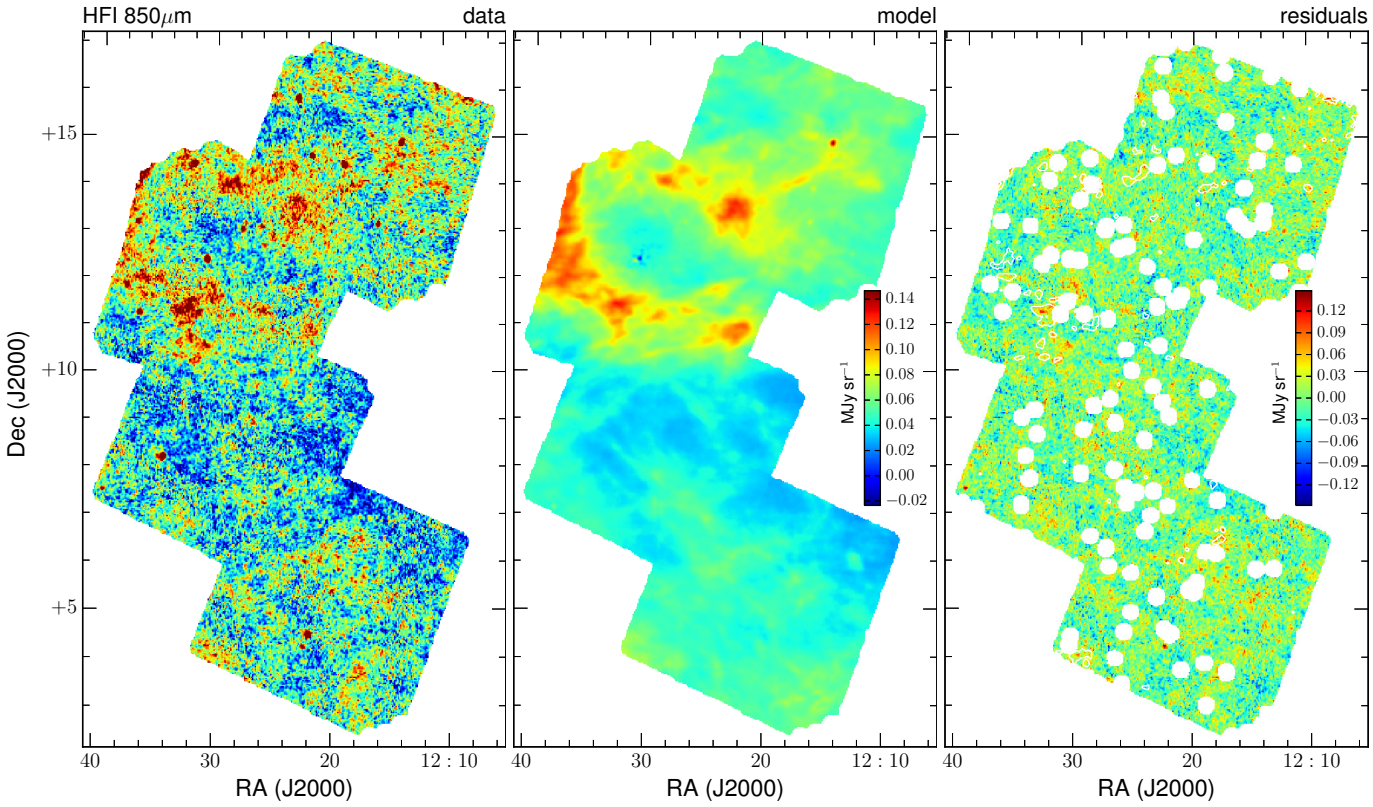

Fig. C.7. Same as Fig. 8, but for the HFI 850 μm band.